The Astronomical Journal, 165:85 (24pp), 2023 March https://doi.org/10.3847/1538-3881/aca8fc

TESS Hunt for Young and Maturing Exoplanets (THYME). IX. A 27 Myr Extended Population of Lower Centaurus Crux with a Transiting Two-planet System

Mackenna L. Wood[1], Andrew W. Mann[1], Madyson G. Barber[1,28], Jonathan L. Bush[1], Adam L. Kraus[2], Benjamin M. Tofflemire[2,29], Andrew Vanderburg[3], Elisabeth R. Newton[4], Gregory A. Feiden[5], George Zhou[6], Luke G. Bouma[7,29], Samuel N. Quinn[8], David J. Armstrong[9,10], Ares Osborn[9,10], Vardan Adibekyan[11,12], Elisa Delgado Mena[11], Sergio G. Sousa[11], Jonathan Gagné[13,14], Matthew J. Fields[1], Reilly P. Milburn[1], Pa Chia Thao[1], Stephen P. Schmidt[1], Crystal L. Gnilka[15,16], Steve B. Howell[15], Nicholas M. Law[1], Carl Ziegler[17], César Briceño[18], George R. Ricker[3], Roland Vanderspek[3], David W. Latham[8], Sara Seager[3,19,20], Joshua N. Winn[21], Jon M. Jenkins[22], Joshua E. Schlieder[23], Hugh P. Osborn[3,24], Joseph D. Twicken[15,25], David R. Ciardi[26], and Chelsea X. Huang[27]

[1] Department of Physics and Astronomy, The University of North Carolina at Chapel Hill, Chapel Hill, NC 27599, USA; woodml96@live.unc.edu
[2] Department of Astronomy, The University of Texas at Austin, Austin, TX 78712, USA
[3] Department of Physics and Kavli Institute for Astrophysics and Space Research, Massachusetts Institute of Technology, Cambridge, MA 02139, USA
[4] Department of Physics and Astronomy, Dartmouth College, Hanover, NH 03755, USA
[5] Department of Physics & Astronomy, University of North Georgia, Dahlonega, GA 30597, USA
[6] Centre for Astrophysics, University of Southern Queensland, West Street, Toowoomba, QLD 4350, Australia
[7] Cahill Center for Astrophysics, California Institute of Technology, Pasadena, CA 91125, USA
[8] Center for Astrophysics | Harvard & Smithsonian, 60 Garden Street, Cambridge, MA, 02138, USA
[9] Department of Physics, University of Warwick, Gibbet Hill Road, Coventry, CV4 7AL, UK
[10] Centre for Exoplanets and Habitability, University of Warwick, Gibbet Hill Road, Coventry, CV4 7AL, UK
[11] Instituto de Astrofísica e Ciências do Espaço, Universidade do Porto, CAUP, Rua das Estrelas, 4150-762 Porto, Portugal
[12] Departamento de Física e Astronomia, Faculdade de Ciências, Universidade do Porto, Rua do Campo Alegre, 4169-007 Porto, Portugal
[13] Planétarium Rio Tinto Alcan, Espace pour la Vie, 4801 av. Pierre-de Coubertin, Montréal, Québec, Canada
[14] Institute for Research on Exoplanets, Université de Montréal, Department de Physique, C.P. 6128 Succ. Centre-ville, Montréal, Québec, Canada
[15] NASA Ames Research Center, Moffett Field, CA 94035, USA
[16] NASA Exoplanet Science Institute, Caltech/IPAC, Mail Code 100-22, 1200 E. California Boulevard, Pasadena, CA 91125, USA
[17] Dunlap Institute for Astronomy and Astrophysics, University of Toronto, 50 St. George Street, Toronto, Ontario M5S 3H4, Canada
[18] Cerro Tololo Inter-American Observatory, Casilla 603, La Serena, Chile
[19] Department of Earth, Atmospheric and Planetary Sciences, Massachusetts Institute of Technology, Cambridge, MA 02139, USA
[20] Department of Aeronautics and Astronautics, MIT, 77 Massachusetts Avenue, Cambridge, MA 02139, USA
[21] Department of Astrophysical Sciences, Princeton University, 4 Ivy Lane, Princeton, NJ 08544, USA
[22] NASA Ames Research Center, Moffett Field, CA 94035, USA
[23] NASA Goddard Space Flight Center, 8800 Greenbelt Road, Greenbelt, MD 20771, USA
[24] Physikalisches Institut, University of Bern, Gesellsschaftstrasse 6, 3012 Bern, Switzerland
[25] SETI Institute, Mountain View, CA 94043, USA
[26] Caltech/IPAC, NASA Exoplanet Science Institute, 770 S. Wilson Avenue, Pasadena, CA 91106, USA
[27] University of Southern Queensland, Centre for Astrophysics, West Street, Toowoomba, QLD 4350, Australia
Received 2022 August 18; revised 2022 November 29; accepted 2022 December 2; published 2023 February 3

Abstract

We report the discovery and characterization of a nearby (∼85 pc), older (27 ± 3 Myr), distributed stellar population near Lower Centaurus Crux (LCC), initially identified by searching for stars comoving with a candidate transiting planet from TESS (HD 109833; TOI 1097). We determine the association membership using Gaia kinematics, color–magnitude information, and rotation periods of candidate members. We measure its age using isochrones, gyrochronology, and Li depletion. While the association is near known populations of LCC, we find that it is older than any previously found LCC subgroup (10–16 Myr), and distinct in both position and velocity. In addition to the candidate planets around HD 109833, the association contains four directly imaged planetary-mass companions around three stars, YSES-1, YSES-2, and HD 95086, all of which were previously assigned membership in the younger LCC. Using the Notch pipeline, we identify a second candidate transiting planet around HD 109833. We use a suite of ground-based follow-up observations to validate the two transit signals as planetary in nature. HD 109833 b and c join the small but growing population of <100 Myr transiting planets from TESS. HD 109833 has a rotation period and Li abundance indicative of a young age (≲100 Myr), but a position and velocity on the outskirts of the new population, lower Li levels than similar members, and a color–magnitude diagram position below model predictions for 27 Myr. So, we cannot reject the possibility that HD 109833 is a young field star coincidentally nearby the population.

[28] UNC Chancellor's Science Scholar.
[29] 51 Pegasi b Fellow.

Unified Astronomy Thesaurus concepts: Stellar ages (1581); Transit photometry (1709); Exoplanets (498); Stellar associations (1582); Stellar kinematics (1608)

Supporting material: machine-readable table

1. Introduction

Young associations—coeval stellar populations thought to share a common age, metallicity, and kinematics—are crucial for studies of stellar and planetary evolution, including circumstellar disk lifetimes (Haisch et al. 2001), planet formation and migration (Mann et al. 2016b; David et al. 2016; Donati et al. 2016), pre-main-sequence (pre-MS) evolution (Stassun et al. 2014; Kraus et al. 2015), and planetary mass loss (Rockcliffe et al. 2021; Zhang et al. 2022). However, the utility of a young association for such studies depends on a robust understanding of the association's structure and properties. In the last decades, detailed surveys of nearby associations have shown a much more complicated picture of the properties, structure, and formation history of stellar associations than previously known.

The advent of the high-precision position, velocity, and color measurements of Gaia (Gaia Collaboration et al. 2016) combined with new techniques for locating associations (e.g., HDBSCAN; McInnes & Healy 2017) have significantly altered our view of young associations near the Sun. One revelation has been the level of subgrouping within well-known associations. For example, Wright & Mamajek (2018) and Krolikowski et al. (2021) found that the distribution of stellar ages and kinematics within large associations is likely the result of many localized star formation events occurring over periods of 5–10 Myr as opposed to the collapse of a single molecular cloud. Some studies have revealed entirely new young populations (Oh et al. 2017; Kounkel et al. 2019), including some that are far more diffuse than those previously known (Meingast et al. 2019). Other studies have found that groups thought to be distinct may be fragments of a single star formation event (Gagné et al. 2021). The new discoveries and changes to known populations create a more complex picture of young associations and change our understanding of the origin of nearby stellar associations (e.g., Zucker et al. 2022).

The Scorpius-Centaurus Association (Sco-Cen) is the nearest OB association to the Sun, harboring $\simeq$150 B-type stars and tens of thousands of lower-mass members (de Zeeuw et al. 1999). The association is classically divided into three populations: Upper Scorpius, Upper Centaurus Lupus, and Lower Centaurus Crux (LCC), with ages varying from 11–17 Myr (Pecaut et al. 2012). The Sco-Cen complex (sometimes called Greater Sco-Cen) includes many other molecular clouds and star-forming groups (e.g., Ophiuchus and Lupus), but none of the main three groups show evidence of ongoing star formation (Preibisch & Mamajek 2008). This combination of factors makes Sco-Cen an exceptional laboratory to test models of early stellar evolution, and has motivated more than a century of intense research (e.g., Kapteyn 1914; Pecaut et al. 2012; Feiden 2016; Wright & Mamajek 2018).

However, there is still much to be understood about the structure and formation of Sco-Cen, particularly with the arrival of astrometry from Gaia (Gaia Collaboration et al. 2016). Pecaut & Mamajek (2016) found a strong age gradient across Sco-Cen in general and LCC in particular, noting that the southern region of LCC is younger than the northern. Goldman et al. (2018) found a separate moving group within the southern portion of LCC, dividing it into multiple subpopulations with ages ranging from 7–10 Myr. This result was confirmed by Kerr et al. (2021), who recovered those four groups and included the younger ϵ Chamaeleontis as a fifth. These discoveries raise the possibility that the census of Sco-Cen is still incomplete.

Mapping out Sco-Cen is particularly important because of its outsized role in the study of young planets. It is nearby and young enough for direct imaging of young planets on wide orbits (e.g., Hinkley et al. 2015; Bohn et al. 2020a). The association is also diffuse enough to separate out individual stars even with large K2 and TESS pixels, enabling the discovery of young transiting planets. The youngest known transiting planet (K2-33 b; David et al. 2016; Mann et al. 2016b), the youngest transiting hot Jupiter (HIP 67522 b; Rizzuto et al. 2020), and the largest planet known to orbit a mid-M dwarf (TOI 1227 b; Mann et al. 2022) are all in Sco-Cen. Such systems are critical to our understanding of the early evolution of planetary systems, but the sample is still small. New substructures in Sco-Cen would provide new regions to search for such planets, potentially with a wider range of (young) ages.

In this paper, we report the discovery of a new, older (27 ± 3 Myr) population outside LCC. Our discovery of the young association was prompted by the detection of HD 109833 b by the TESS survey. The host, HD 109833, was included as a member of the Theia 64 moving group by Kounkel et al. (2019) and a member of the Sco-Cen region by Kerr et al. (2021). After confirming indicators of youth in HD 109833 (see Section 6), we searched its nearest kinematic and spatial neighbors to see if they also appeared to be in a young association. The resulting color–magnitude diagram (CMD) showed a significant population of pre-main-sequence M dwarfs, indicating a young ($<$50 Myr) association. We investigate the age and membership of this association and its relationship with existing Sco-Cen populations and statistically validate the planet candidates HD 109833 b and c.

In Section 2, we describe our iterative process for locating members and removing field and LCC interlopers. We discuss our observational program in Section 3, with observations both of the planet host and the association members. We describe the properties of the association, including its age, in Section 4, and some notable directly imaged planet-hosting candidate members in Section 5. Section 6 discusses the properties of the planet host HD 109833, and Section 7 discusses the properties of the planets. We conclude in Section 8 with a summary of our work and brief discussion of the implications of this new population.

2. The Membership of the MELANGE-4 Association

In this Section, we attempt to confirm that the population of stars spatially and kinematically near HD 109833 is part of a real, coeval association and to separate out interlopers from nearby LCC populations and the field. As we show later, this does not appear to be part of a known group, so we refer to the association as MELANGE-4 following the naming convention from Tofflemire et al. (2021).

To select the membership of MELANGE-4 we use an iterative four-step process, using a mix of kinematic and age-based indicators of membership. During the first two steps, our goal is to produce a clean membership list, preferring to exclude member stars than to include nonmember stars. We then use that clean list to define the properties of the group. This initial list is used to define the group's kinematics for a more expansive search for members in the next two steps. This process is outlined below, and detailed in Sections 2.1–2.4.

1. Initial Selection—we select nearby comoving stars using the `Comove` algorithm.
2. Remove Interlopers—we apply cuts to the initial candidate list using color, magnitude, and rotation to remove interlopers from LCC and the field.
3. `BANYAN` Σ—we use the refined candidate list to define the group kinematics, then use `BANYAN` Σ and full 6D kinematics (or 5D for those lacking a radial-velocity (RV) measurement) of each candidate to determine kinematic membership probabilities and search for additional candidate members.
4. Reapply Cuts—We reapply the color and magnitude cuts to the kinematic candidates. This produces the final candidate list, comprising stars that are clustered in color, magnitude, kinematics, and rotation.

We note that these steps inevitably create some biases in the list. For example, the use of colors and magnitudes to select members may bias the age (depending on how the cuts are applied). For this reason, we provide the candidate membership lists from each step so that readers can apply their own cuts on the data based on the specific scientific case.

2.1. Initial Selection

We initially select the comoving neighbors of HD 109833 using `Comove`.[30] Details of the algorithm are given in Tofflemire et al. (2021). To summarize, `Comove` uses astrometry from the Gaia Data Release 3 (DR3; Lindegren et al. 2021; Riello et al. 2021; Gaia Collaboration et al. 2022) and a user-provided velocity of HD 109833 to compute its *XYZ* position, and *UVW* velocity.[31] `Comove` then selects every Gaia star within a user-defined threshold of HD 109833 in 3D distance and expected tangential velocity ($V_{t,\mathrm{exp}}$) assuming a *UVW* matching HD 109833. We opted to use thresholds of 30 pc and 2 km s^{-1}. This tight limit likely removes many real members (particularly fainter stars with tangential velocity uncertainties larger than 2 km s^{-1}), but larger search radii led to significant contamination from younger LCC stars. From this sample, we took those that had valid Gaia B_P and R_P magnitudes, yielding an initial selection of 207 stars, shown in Figure 1.

In addition to Gaia astrometry, velocities, and photometry, we retrieve the Gaia renormalized unit weight error (RUWE) for each candidate member star. The RUWE value is related to the goodness-of-fit from the Gaia astrometry, normalized to correct for color and brightness dependent effects.[32] The RUWE should be around 1 for well-behaved sources, and higher values suggest the presence of a stellar companion (Ziegler et al. 2018; Belokurov et al. 2020; Wood et al. 2021).

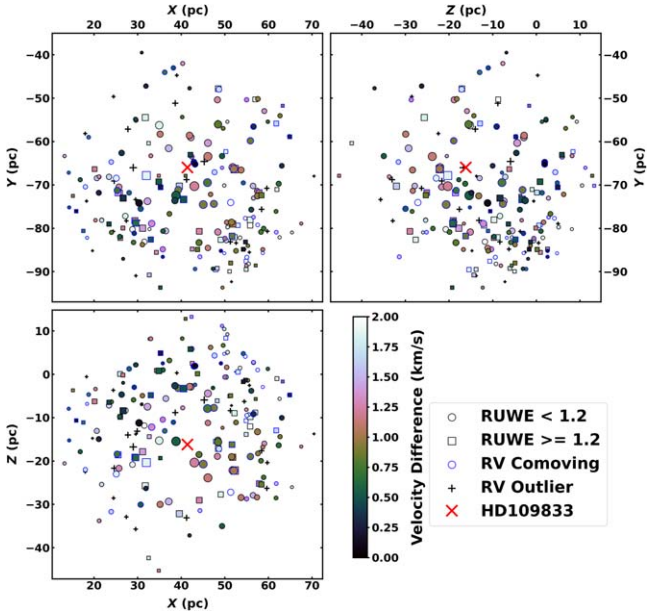

Figure 1. The results of `Comove`. HD 109833 and neighbors within 30 pc and 2 km s^{-1}, are shown in *X*-, *Y*-, and *Z*-coordinates. The size of the points corresponds inversely to their distance from HD 109833, and the color with the velocity difference, so that the largest points are closest to HD 109833, and the darkest points are most similar in velocity. Stars with Gaia renormalized unit weight error (RUWE) $\geqslant 1.2$ are represented with squares. The velocity differences of binary stars are poor indicators of membership, due to velocity from binary motion. Circles are used to represent stars with Gaia RUWE < 1.2.

The selection reveals a population of pre-MS stars close to HD 109833 in both position and velocity (Figure 2), indicating a young comoving population. We use this population as our initial membership list. However, it includes many stars that do not appear to be a part of the main population (e.g., main-sequence, MS, field interlopers). To remove these probable interlopers, we make a series of cuts on the initial list.

2.2. Removing LCC and Field Interlopers

We make four cuts on the initial sample of candidate members, divided into those meant to remove LCC interlopers and those meant to remove field interlopers. Nearby members of LCC are young, so they cannot be distinguished from this population by CMD position or other age-based qualities, but are kinematically distinct. In contrast, nearby field stars may have similar position and motion to population members, but are unlikely to be young and thus can be identified through differences in age indicators.

For our first cut, we use the empirical MS defined in Pecaut & Mamajek (2013). We remove all candidates that have $B_P - R_P > 1$, $G - R_P > 0.5$ and are fainter than the interpolated empirical MS (Figure 2). This removes 28 candidates. The anomalous CMD positions of some of these stars are likely caused by poor B_P magnitude and parallax measurements from Gaia, but those are still "contaminants" from the perspective of our analysis, as including them would bias estimates of the group's age.

The rotation period of a star can also be used as an indicator of age since stars are known to "spin down" with increasing age. To this end, we measure the rotation periods of 166 candidate members using the Lomb-Scargle periodogram of

[30] https://github.com/adamkraus/Comove

[31] This is using a galactic coordinate system in which the Sun is at $\langle 0, 0, 0 \rangle$, *X* points toward the galactic center, *Y* is in the direction of galactic rotation, and *Z* is out of the galactic plane. *U*, *V*, and *W* are the velocities in the *X*-, *Y*-, and *Z*-directions, respectively.

[32] https://gea.esac.esa.int/archive/documentation/GDR2/Gaia_archive/chap_datamodel/sec_dm_main_tables/ssec_dm_ruwe.html

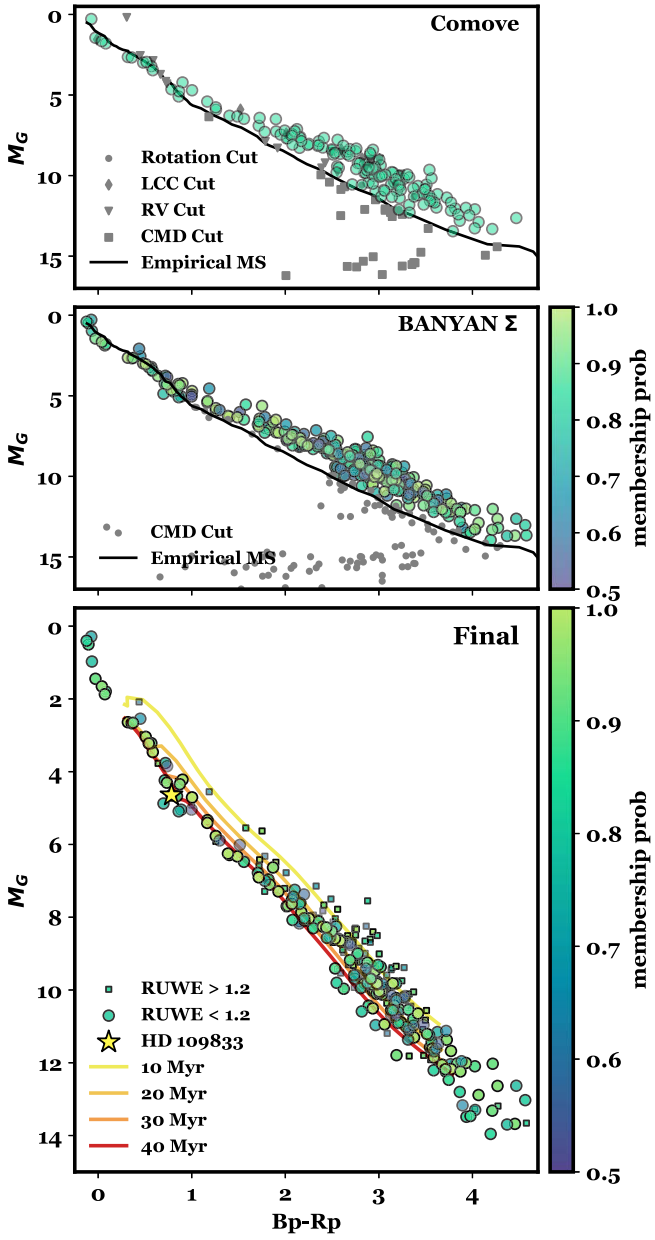

Figure 2. A CMD showing each step of the membership search. The top panel shows the results of Comove, and the cuts made on those results to make a tight core membership. The second panel shows the results of BANYAN Σ and the subsequent cut on CMD position to remove old interlopers and stars with poor color measurements. Candidates that survived this cut are colored by their kinematic membership probability. The bottom panel shows the final membership list, colored by membership probability. Stars with Gaia RUWE > 1.2, possible binaries, are marked as small squares, and form a binary sequence above the main association. Four DSEP magnetic isochrones (Feiden 2016), showing 10, 20, 30, and 40 Myr, are plotted alongside the sequence. In the top two panels, the zero-age main sequence is shown as a black line, derived empirically by Pecaut & Mamajek (2013).

TESS light curves (see Section 4.2 for more details). We remove any stars that have high-quality TESS data, but do not show a reliable rotation period. Stars with TESS magnitude $T > 15$ are not removed, since they are too faint to have adequate signal-to-noise ratios (S/Ns) for rotation measurement, and thus we cannot reject them as members, as our goal here is to remove only those that we are confident are not members. A total of eight candidates show no reliable rotation, of which four also had a low CMD position (and hence are removed by the cut above).

We remove 18 candidates with Gaia DR3 radial velocities >5 km s^{-1} from the values predicted by Comove, and radial-velocity errors <3 km s^{-1}. These stars may be binaries that are genuine members, but we err on the side of a clean rather than a complete sample.

Lastly, to remove interlopers from the nearby LCC populations, we cross-match our candidate list against the membership list from Goldman et al. (2018), and remove all candidates that are considered LCC members in that paper. We remove five stars for this reason, with an additional Goldman member removed by the earlier velocity cut. It is possible that these stars, which were believed to be members of one of the LCC subpopulations, are actually members of MELANGE-4, but at this stage, the goal is to get a clean list even at the cost of removing some true members.

These steps are outlined in the top panel of Figure 2. The cuts give a final sample of 152 candidate members.

2.3. BANYAN

The Comove selection has a sharp radius cutoff, which misses more distant (spatially and kinematically) stars and gives us only general information about the relative probability that a given star is a member. Once a general sense of the spatial distribution is known, a better approach is to use Bayesian membership probabilities that weight the relative likelihood that a star is within MELANGE-4 compared to the field or a nearby association (Rizzuto et al. 2011; Malo et al. 2012).

To this end, we use the BANYAN Σ tool. BANYAN Σ is a Bayesian probability tool to determine membership probabilities of stars in young moving groups (Gagné et al. 2018).[33] For each star, BANYAN Σ computes the membership probability using kinematic models of 27 nearby, young moving groups defined in Gagné et al. (2018) and the field population.

Significant substructure has been discovered within the LCC association since the publication of BANYAN Σ, and is not accounted for there, so to correctly select members of MELANGE-4, we use updated parameters for the nearby LCC subpopulations in BANYAN Σ. This update is detailed in Appendix A.

We add MELANGE-4 to BANYAN Σ following Gagné et al. (2018) by calculating the covariance matrix and center vector of the candidate members that survived all cuts from Section 2.2, and had Gaia DR2 radial-velocity measurements. These are, in units of parsecs and kilometers per second:

$$\bar{\bar{\Sigma}} = \begin{bmatrix} 152.32 & 30.929 & 12.03 & 2.813 & 8.634 & 1.424 \\ 30.929 & 143.941 & -22.231 & -0.124 & 4.127 & -1.1 \\ 12.03 & -22.231 & 86.511 & 3.7 & -1.383 & -1.119 \\ 2.813 & -0.124 & 3.7 & 2.732 & -3.434 & -0.535 \\ 8.634 & 4.127 & -1.383 & -3.434 & 7.304 & 1.027 \\ 1.424 & -1.1 & -1.119 & -0.535 & 1.027 & 1.048 \end{bmatrix}$$

$$\bar{x}_0 = [42.238 \quad -69.627 \quad -8.228 \quad -9.386 \quad -20.475 \quad -5.596].$$

Using the updated *UVWXYZ* matrix for MELANGE-4 and LCC subpopulations, we run BANYAN Σ on all stars within 100 pc of HD 109833 with a Gaia DR3 parallax and a parallax over error of >20. There may be stars beyond this range, but those more distant stars may require a more sophisticated model than

[33] https://github.com/jgagneastro/banyan.sigma

the multivariate Gaussians used by BANYAN Σ, and we expect this to be a negligible fraction of the overall population at such a young age.

BANYAN Σ yielded 424 candidate members with membership probability greater than 50%. Of the original 152 stars found by Comove, 122 are included in the BANYAN Σ results. There are 168 candidate members with membership probability greater than 90%, which we consider high-probability members. These kinematic candidate members are shown in the middle panel of Figure 2.

2.4. Final Membership

Since BANYAN Σ only considers kinematic information when determining membership probabilities, it is possible that old interlopers, which match the association in *UVWXYZ* but not in age, are included in the membership list. As with our initial selection from Comove, the BANYAN Σ selection includes a large number of stars that are below the main sequence. Therefore, we reapply the CMD cut discussed in Section 2.2. We also remove 20 stars without Gaia Bp or Rp measurements. In total, this step removes 118 stars, yielding a final membership list of 306 stars. Many of these targets may be real members with poor magnitudes or parallaxes. The final membership is shown in the last panel of Figure 2. Their membership probabilities and stellar properties are listed in Table 5.

3. Observations and Reduction

Below we describe observations of both HD 109833 and candidate members of the parent association. The goal of the former was to characterize the host star and the candidate transiting planets. The latter set of observations focused on confirming membership and measuring the age and kinematic properties of the association. For details of how the sample of 306 candidate association members are identified, see Section 2.

3.1. TESS Photometry

We use TESS photometry to measure the transit properties and to measure rotation periods for the planet host and association members. We use different light-curve extractions for these two purposes, as described below.

3.1.1. Observations of the Planet Host

The planet host, HD 109833 (TIC 360630575, TOI 1097), was observed by the TESS mission (Ricker et al. 2015) from 2019 April 22 through 2019 June 18 (Sectors 11 and 12), then again from 2021 April 29 through 2021 June 24 (Sectors 38 and 39). The first two sectors have 30 m cadence data, and Sectors 38 and 39 have 20 s, 2 m, and 10 m cadence data. We employed the 30 m data from the first two sectors and the 20 s data from the last two sectors in this work.

We retrieve light curves for the planet host and candidate members of the parent association from the Mikulski Archive for Space Telescopes (MAST[34]). For analysis of the planet host, we use the Presearch Data Conditioning Simple Aperture Photometry (PDCSAP; Smith et al. 2012; Stumpe et al. 2012, 2014) TESS light curve produced by the Science Processing Operations Center (SPOC; Chiozzi et al. 2016).

[34] https://mast.stsci.edu/portal/Mashup/Clients/Mast/Portal.html

3.1.2. Observations of Association Members

The PDCSAP reduction can weaken long-term trends in the light curve, which favors exoplanet discovery, but impedes measuring rotation periods beyond ≃10 days. So, to measure the rotation periods of candidate association members, we extract light curves from TESS full-frame images using Causal Pixel Models (CPMs; Wang et al. 2016) with the unpopular package (Hattori et al. 2021). Parameters for running unpopular are identical to those described in Barber et al. (2022). We do not extract light curves for stars that were too faint ($T > 15$) or too contaminated by nearby stars (contratio >1.6). In total, we are able to extract usable light curves for 203 of the 306 candidate members. All of the TESS light curves used in this paper can be found in MAST:10.17909/4cwh-0n56.

We use the resulting TESS CPM light curves to measure single-sector rotation periods for stars. For each individual star, we search for periods from 0.1–30 days using a Lomb-Scargle periodogram (Lomb 1976; Scargle 1982; Press & Rybicki 1989). While we search up to 30 days, only stars with $P_{\rm rot} < 12$ days are considered, as the narrow observing window of TESS (27 days) makes longer periods unreliable. We perform an eye check following Rampalli et al. (2021), assigning Quality 0 for clear spot-modulated light curves, Quality 1 to clearly young stars with some ambiguity in their periodogram peaks, Quality 2 to spurious measurements, and Quality 3 to complete nondetections. We visually remove eclipsing binary signals and targets with blended light curves (not all get captured by our contamination ratio requirements). If multiple sectors are available, we report the average of the single-sector measurements after clipping ones that disagree with the clearest signal (strongest Lomb-Scargle power) by more than 25% to eliminate double or half harmonics. Out of 185 candidate members with usable light curves, we assign Quality 0 or 1 to 173 stars.

3.2. High-contrast Imaging

We use high-contrast imaging to search for close companion stars to HD 109833. The data we use can be found on ExoFOP-TESS (https://exofop.ipac.caltech.edu/tess/target.php?id=360630575).

3.2.1. ZORRO/Gemini

To search for close companion stars that might dilute the transit signal, we observed HD 109833 on 2020 March 13 UT with the Gemini South speckle imager, Zorro (Scott et al. 2021). We used the standard speckle imaging mode with narrowband 562 nm and 832 nm filters. The 'Alopeke-Zorro instrument team took all data as part of their program queue operations and reduced the data with their standard pipeline (Howell et al. 2011).

No close companions are detected in either band. The 832 nm filter sets stronger contrast limits, ruling out equal-mass companions at separations $\rho > 0\farcs05$, additional companions with $\delta 832 < 4.6$ magnitudes at $0\farcs1$, and with increasing contrast sensitivity from there out to $\rho = 1\farcs2$.

3.2.2. HRCam/SOAR

We also search for previously unknown companions to HD 109833 using data from the Southern Astrophysical Research Telescope (SOAR) speckle imaging camera (HRCam; Tokovinin 2018) taken on 2020 February 10 UT. Observations

Table 1
RV Measurements of HD 109833

Telescope	BJD UT	RV km s^{-1}
HARPS/La Silla	2458858.8137	10.563 ± 0.002
HARPS/La Silla	2458859.8226	10.598 ± 0.003
HARPS/La Silla	2458861.8281	10.571 ± 0.002
HARPS/La Silla	2458862.8580	10.614 ± 0.003
HARPS/La Silla	2458863.8108	10.548 ± 0.002
HARPS/La Silla	2458864.8653	10.577 ± 0.002
HARPS/La Silla	2458865.8660	10.603 ± 0.002
CHIRON/SMARTS	2459240.8846	10.577 ± 0.052
CHIRON/SMARTS	2459306.7098	10.568 ± 0.03
CHIRON/SMARTS	2459308.7235	10.689 ± 0.064
CHIRON/SMARTS	2459312.6771	10.621 ± 0.04
CHIRON/SMARTS	2459314.7458	10.576 ± 0.042
CHIRON/SMARTS	2459322.7661	10.528 ± 0.058
CHIRON/SMARTS	2459337.6306	10.646 ± 0.083
CHIRON/SMARTS	2459338.6142	10.558 ± 0.115
CHIRON/SMARTS	2459339.6936	10.573 ± 0.053
CHIRON/SMARTS	2459346.5901	10.571 ± 0.074
CHIRON/SMARTS	2459742.5434	10.599 ± 0.037
NRES/LCO	2459672.5589	10.757 ± 0.138
NRES/LCO	2459673.5576	10.809 ± 0.203
NRES/LCO	2459675.6047	10.917 ± 0.162

Note. Measured radial velocities of HD 109833. A 1.4 km s^{-1} offset was added to the measurements from CHIRON/SMARTS in accordance to the zero-point of that instrument.

were taken using the *I* band. As with the Zorro data, we detect no companions in the HRCam data out to $\rho = 3''$. Companions with $\delta I < 1$ are ruled out for $\rho > 0.''1$, and those with $\delta I < 4.5$ ruled out at $\rho > 0.''25$.

3.3. Spectroscopy

To confirm membership in the association and measure the association's age, we gather spectra of candidate association members. Our goals are to estimate the equivalent width (EW) of the Li I 670.8 nm line. The extracted EWs are given in Table 5.

We also obtain spectra of HD 109833 over 3 yr with the goal of checking for signs of binarity. Our analysis of the resulting velocities, detailed in Section 7.3, shows no evidence of binarity. All radial velocities, organized by instrument, are given in Table 1.

3.3.1. Goodman/SOAR Spectroscopy

We observe a total of 26 candidate association members using the Goodman High Throughput Spectrograph (Clemens et al. 2004). Goodman is part of SOAR atop Cerro Pachon, Chile. Observations were taken over eight nights between 2021 March 29 and 2021 September 20, under mostly photometric conditions.

From the list of candidate association members, these 26 are selected for observation with the goal of mapping out the lithium-depletion boundary (LDB). To choose stars to observe, we estimate the age of the association from an isochrone, and use that age to predict the magnitude of the LDB in M_{Ks}. We then select stars with $\Delta K < 1$ from the predicted boundary. This estimate was updated as we took more data and revised the age of the group, so there was no single observing list. We choose stars for observing based on their magnitude in Gaia R_P (prioritizing brighter stars that need shorter exposures), Gaia RUWE (omitting stars with RUWE > 1.2 as they are more likely to be binaries), and location on sky (prioritizing short slews between targets and middle elevations).

Observations were designed to measure the EW of the Li I 670.8 nm line; we use the red camera, the 1200 l/mm grating, and the M5 mode, which provides a wavelength coverage of 630–740 nm. We use either the 0.45″ slit, or the 0.6″ slit, depending on the magnitude of the target and atmospheric seeing. This setup should give a resolution of $R = 4500$–5800, although in practice the true resolution is lower and varies with exposure time (see below). For each target, we take five spectra with exposure times varying from 10–300 s each.

For reduction, we perform standard bias subtraction, flat-fielding, and optimal extraction of the target spectrum. The spectra show large wavelength shifts while observing, likely due to issues with the mount model and flexure compensation system. In extreme cases, this shifts the spectrum by 5–10 pixels between exposures of the same target, which corresponds to several resolving elements (depending on the slit). To mitigate the effect, we take Ne arcs prior to each target and use simultaneous skyline spectra to calibrate the wavelength solution of individual spectra. The combination of a pre-target arc and sky lines performs better than bracketing the data with arcs. We make an initial map of pixels to wavelengths using a fourth-order polynomial derived from the nearest Ne arc, then apply a linear correction to each spectrum based on the sky lines. We stack the extracted and wavelength calibrated spectra using a robust weighted mean. The stacked spectra have mean S/N > 40 for all targets.

We correct each star to its rest wavelength using radial-velocity standards taken with the same setup. Although the resulting spectra were sufficient for spectral typing and measuring relevant EWs (e.g., EW[Li]), we find the radial velocities to be poor ($\sigma_{rv} \simeq 5$–10 km s^{-1} based on stars with known velocity). This is likely due to nonlinearity in the wavelength shifts impacting the edges of the spectrum and regions with fewer sky lines and nonuniform shifts during an exposure. As a result, we do not report velocities based on these spectra.

3.3.2. NRES/LCO

To increase the baseline of our RV characterization of HD 109833, we obtain three spectra of HD 109833 using the Network of Robotic Echelle Spectrographs (NRES; Siverd et al. 2018) at the Las Cumbres Observatory (LCO). Observations were taken the nights of 2022 April 3, 4, and 5.

NRES spectra cover 380–860 nm at high resolution ($R \sim 53{,}000$). The data are reduced using the LCO NRES pipeline `BANZAI-NRES`.[35] This includes extraction of radial velocities by cross-correlating observed spectra with PHOENIX model atmospheres (Husser et al. 2013).

3.3.3. HARPS

For RV characterization of the planet host HD 109833, we also obtain seven spectra of that star taken with the High Accuracy Radial velocity Planet Searcher (HARPS) fiber-fed

[35] https://github.com/LCOGT/banzai-nres

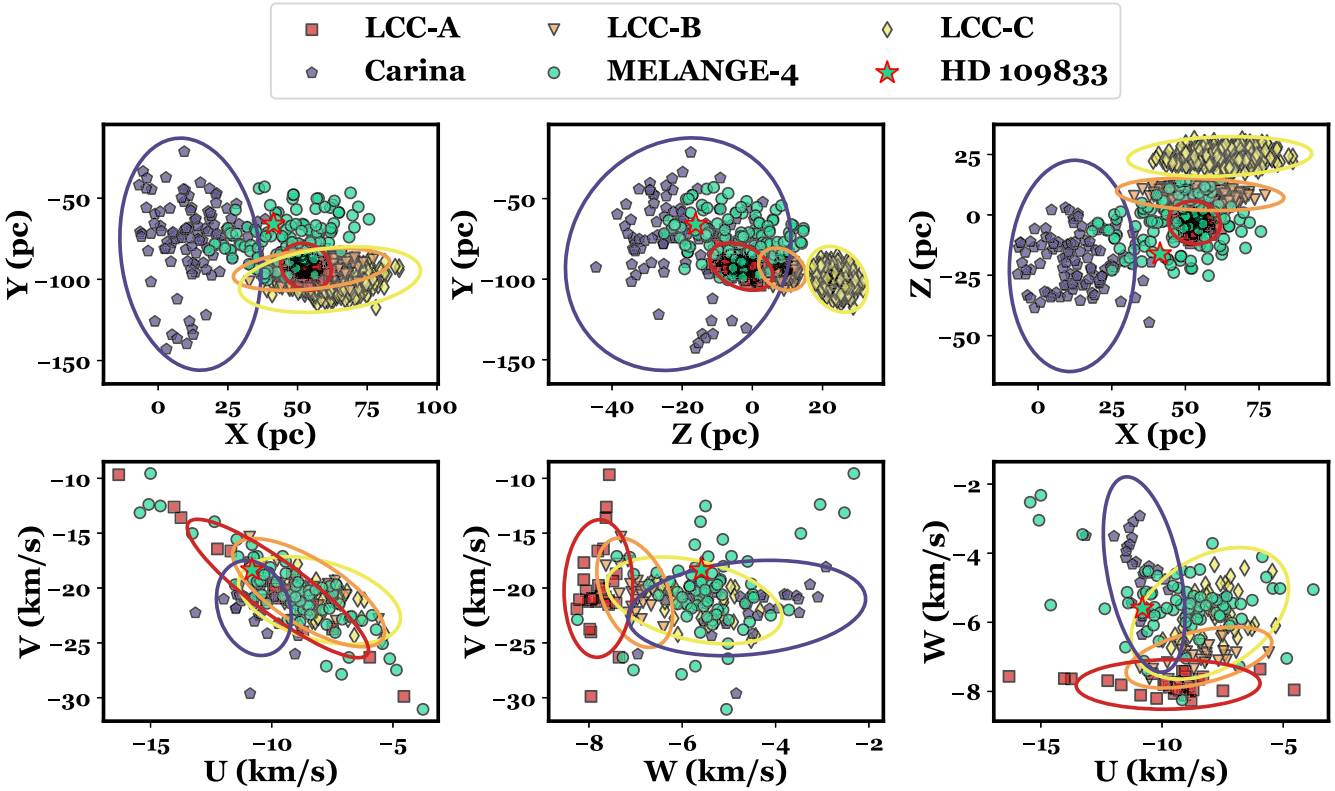

Figure 3. The spatial and velocity spreads of MELANGE-4, the nearby LCC subpopulations, and Carina. The top row shows the galactic position (X, Y, and Z) for each population, and the bottom row shows the velocities (U, V, and W). The membership candidates for MELANGE-4 are shown in turquoise, and high-probability (>99%) members of LCC-A, LCC-B, LCC-C, and Carina are shown in red, orange, yellow, and purple, respectively. The position of HD 109833 is marked with a turquoise star.

Echelle Spectrograph on the ESO 3.6 m telescope at La Silla Observatory under the NCORES large program (ID 1102.C-0249, PI: Armstrong). The spectra are high resolution ($R \sim 115{,}000$), and cover a spectral range of 378–691 nm. Observations were taken on the nights of 2020 January 10–11 and 13–17 in high-accuracy mode, with an exposure time of 1500–1800 s, depending on observing conditions, and a typical S/N per pixel of 100. The standard online HARPS data reduction pipeline reduces the data, using a G2 template to form the weighted cross-correlation function to determine the RVs. We find a typical error on the RVs of 2–3 m s^{-1}.

3.3.4. CHIRON/SMARTS

We acquire 12 spectra of HD 109833 using CHIRON at the SMARTS 1.5 m telescope at Cerro Tololo Inter-American Observatory (Tokovinin et al. 2013). These observations were acquired between 2021 January 26 and 2022 June 12. We use CHIRON in its image slicer mode, which gives a resolution of $\approx -79{,}000$ across $415 - 880$ nm.

We also acquire spectra of two MELANGE-4 candidate members on 2021 April 30, and 2021 May 4 using the same setup and reduction.

To derive the radial velocities and stellar parameters for the 11 spectra that met our signal-to-noise requirements, we follow the methods described in Zhou et al. (2018). We perform a least-squares deconvolution of the spectra using nonrotating synthetic spectral templates (Donati et al. 1997). These templates are constructed using the ATLAS9 atmosphere models (Castelli & Kurucz 2004) and the SPECTRUM script (Gray & Corbally 1994). The resulting line profiles were fit using a broadening kernel that included terms for the rotational, macroturbulent, and instrumental broadening. We then fit the line profile from each observation independently, yielding the radial velocities listed in Table 1, as well as a mean rotational broadening velocity of $v \sin i_\star = 10.5 \pm 0.2$ km s^{-1}.

4. Properties of the MELANGE-4 Association

4.1. MELANGE-4 in the Context of nearby Associations

The central position and velocity of MELANGE-4 is near the LCC population on the southern part of Sco-Cen and is on the western edge of the Carina association. Despite its proximity to these populations, the positions and velocities of members make it clear that MELANGE-4 is not part of any known associations. This is demonstrated in Figure 3 and described in further detail below.

Recent research has split LCC into four subpopulations (Goldman et al. 2018; Kerr et al. 2021), which we consider separately. Goldman et al. (2018, hereafter G18) found four subpopulations: LCC-A0, LCC-A, LCC-B, and LCC-C, from youngest to oldest. The same subpopulations were found by Kerr et al. (2021, hereafter K21), where they were named LCC-B, LCC-C, LCC-E, and LCC-D, respectively. We use the names from G18, and focus on LCC-A, LCC-B, and LCC-C, as these are the most well defined. LCC-A0, which is renamed as the Musca association by Mann et al. (2022), is the youngest of the subpopulations (11 ± 2Myr), and the farthest from MELANGE-4. See Appendix A for details on these subpopulations.

MELANGE-4 shows significant spatial overlap with LCC-A and partial spatial overlap with LCC-B, but is completely separate from both subpopulations in W. In terms of velocity, it

overlaps partially with LCC-C, from which it is farthest in *XYZ*. Only three to four stars in our list of candidate members of MELANGE-4 overlap with a single LCC group in both *XYZ* and *UVW* (the sources with the most negative W in Figure 3). As expected, these have the lowest membership probabilities (50%–60%). As we show later in this Section, the age of MELANGE-4 is also significantly older than the closest LCC subgroups.

In addition to the LCC subgroups, MELANGE-4 has kinematic overlap with the Carina association. However, the mean X of MELANGE-4 is $\simeq$40 pc from the center of Carina. Similarly, most age estimates for Carina find an age of $\simeq$40 Myr (e.g., Torres et al. 2008; Bell et al. 2015; M. L. Wood et al. 2022, in preparation), which are inconsistent with the age we find for MELANGE-4. Booth et al. (2021) found a younger age for Carina ($\simeq$15 Myr), but this is still inconsistent with our age of MELANGE-4.

One thing that stands out is how diffuse the group is in *XYZ* space compared to known LCC populations. This makes it look like a group transitioning from the more tightly packed population within large complexes toward the more diffuse moving groups (e.g., Kraus et al. 2017). The broad distribution can explain why the group was not noticed prior to the arrival of Gaia data, as well as why many members were previously thought to be part of LCC or Carina.

4.2. Age from Rotation

The rotation sequence can be used to constrain the age of a population (e.g., Tofflemire et al. 2021; Andrews et al. 2022; Newton et al. 2022; Messina et al. 2022). For $<$100 Myr associations, this is more challenging because many late-type stars are still spinning up as they contract onto the main sequence and Sun-like or warmer stars have not yet moved onto the slow-rotating sequence (Rebull et al. 2018). However, the *spread* in rotation periods within a group is still a useful proxy for age. For example, the period spread in 10 Myr Upper Sco is much greater than for 40–60 Myr associations like Tucana-Horologium and μ Tau (Gagné et al. 2020) because the rotation spread at 10 Myr is driven mostly by initial rotation rather than sculpting effects.

We show the rotation distribution of candidate members of MELANGE-4 with Quality 0 or 1 periods alongside other young populations in Figure 4. As expected, low-mass members are rotating slower than slightly older stars as they are still spinning up while contracting toward the main sequence. Similarly, the higher-mass members contain a mix of rapidly rotating stars and those that have started to move to the slow-rotating sequence. The overall rotation distribution is consistent with a 20–40 Myr population.

4.3. Age from Lithium Depletion

Li is rapidly burned in the core of most stars, and for fully convective stars on the main sequence (early M and later) there is an age-dependent cutoff in $T_{\rm eff}$ above which all Li has been consumed and below which the stars retain nearly all initial lithium known as the LDB. The LDB is sharp, generally providing a more precise age measurement than isochrones or rotation (Burke et al. 2004). The location of the LDB is less sensitive to model assumptions, which makes the LDB a "semifundamental" age estimator (Soderblom et al. 2014).

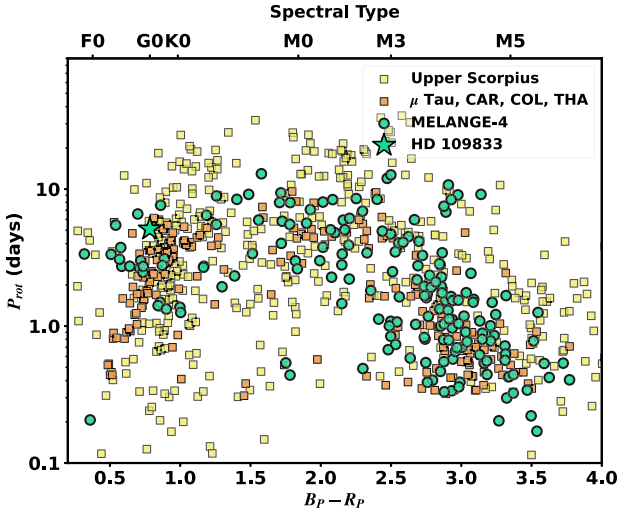

Figure 4. Rotation periods of candidate members of MELANGE-4 as a function of Gaia $B_P - R_P$ color. We compare the color–period sequence of candidate members to the younger ($\sim$10 Myr) population of Upper Scorpius (Rebull et al. 2018) and older (45–60 Myr) populations of Carina (CAR), Columba (COL), Tucana-Horologium (THA), and μ Tau (Gagné et al. 2020). As expected, the MELANGE-4 sequence shows more coherence than the sequence of the younger Upper Scorpius. The low-mass candidates rotate slower than those in the 45–60 Myr populations, indicating a younger population that will spin up as they contract onto the main sequence. The high-mass candidates are a mix of still rapidly rotating stars and stars that have begun to spin down.

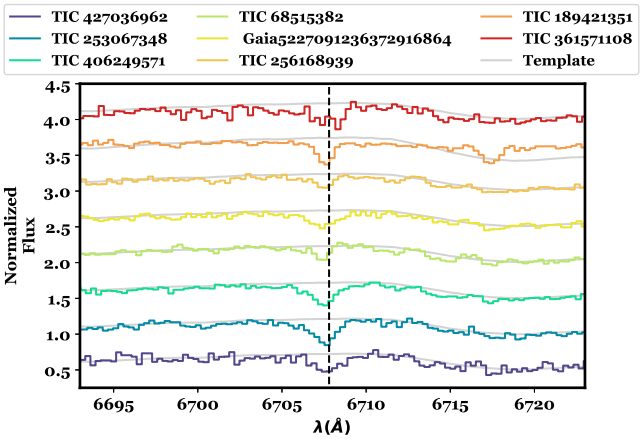

Figure 5. Spectra of all association members with measured Li absorption, overplotted with a Li free M-dwarf template (gray; Bochanski et al. 2007). The location of the Li line, 6707.8 Å, is marked with a dashed black line. Two of these stars, TIC 68515382 (light green) and TIC 256168939 (light orange), have EW(Li) $<$ 300 mÅ, and thus are not fully Li-depleted.

We measure the LDB age of the association using the SOAR/Goodman spectra described in Section 3.3.1. We estimate the EW of the Li I 670.8 nm line (EW[Li]), using a pseudo-continuum estimate from a linear fit to the region on either side of the line. To account for variations in the line width ($v \sin i_*$ and resolution differences between spectra), we manually adjust the width of Li region to include both line edges. Spectra of all association members with measured Li absorption are shown in Figure 5. Our analysis does not account for contamination from the nearby Fe line (6707.4 Å) in the FGK stars nor molecular contamination of the continuum in the cooler M dwarfs. As a result, the uncertainties are likely

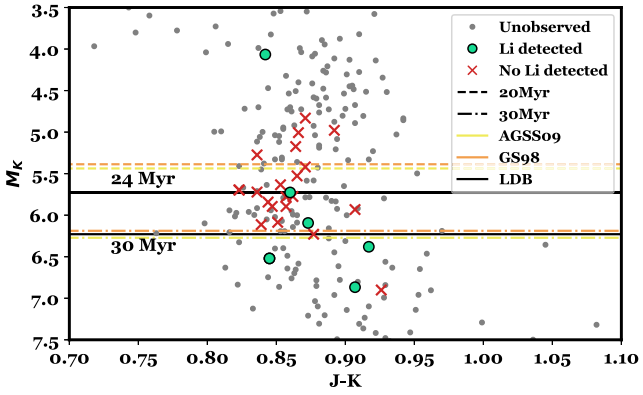

Figure 6. The lithium-depletion boundary (LDB) of MELANGE-4. Shown is the color ($J-K$) and absolute magnitude (K_s) of members of MELANGE-4. Observed stars with EW(Li) > 300 mÅ are shown as colored dots, and stars with EW(Li) < 300 mÅ as red X's. Candidate association members that were not observed are shown as gray dots. Orange and yellow lines show the predicted 20 and 30 Myr 99% LDBs using the DSEP magnetic models with two different solar abundances. The 30 Myr GS98 line has been moved up by 0.03 magnitudes to increase visibility. The solid black lines through the brightest M-dwarf with Li absorption, and the faintest likely member without Li absorption show the edges of the boundary region.

no better than 10% independent of S/N. The EWs are listed in Table 6 and plotted in Figure 7.

To locate the LDB we must define a threshold between Li-rich and Li-poor stars. We have chosen a threshold of EW[Li]$\geqslant$ 300 mÅ, following the reasoning of Binks et al. (2021), and using the curve of growth from Zapatero Osorio et al. (2002). As a proxy for stellar mass or $T_{\rm eff}$, we use the absolute K_S-band magnitudes from the Two Micron All Sky Survey (2MASS) with parallaxes from Gaia DR3. K_S is less sensitive to metallicity (Mann et al. 2019), reddening, and spots (Somers et al. 2020) than Gaia colors, and is broadly available for our targets.

As expected, we identify a region above which no Li is present and below which all high-probability members have Li (see Figure 6). The single star with a Li detection at $M_K = 4$ (TIC 189421351) is more massive than the other stars and is expected to have undepleted Li (see Figure 7). The star with no detected Li and $M_K = 6.9$ (TIC 443273186) has a low CMD position and is a likely field interloper, so we exclude it from this analysis. The upper boundary of this region is defined as the magnitude of the brightest star that we have observed to have pEW(Li) > 300 mÅ, and the lower boundary by the magnitude of the faintest star with pEW(Li) < 300 mÅ. Using that definition, we find that the LDB region spans $5.7 < M_K < 6.1$. Using a more generous definition of 200 mÅ for Li-rich (e.g., Binks & Jeffries 2014) adds one additional Li-rich star at $M_K = 5.9$. This did not affect our LDB region or measured age.

We determine the age of MELANGE-4 by comparing this LDB location to several stellar evolution models with varying assumptions (e.g., magnetic field strength and spot coverage). For each model, we define the LDB as the magnitude at which Li has been depleted from the initial amount by 99%. We use isochrones taken from Baraffe et al. (2015, hereafter BHAC15), and the Dartmouth Stellar Evolution Program (DSEP; Dotter et al. 2008) as our baseline models. For the treatment of magnetic fields, we use isochrones from Feiden (2016), which are built on top of the DSEP models. The magnetic DSEP models include grids built on two different sets of solar abundances, from Grevesse & Sauval (1998, hereafter GS98), and Asplund et al. (2009, hereafter AGSS09). These different abundance scales produce slightly different predictions for Li depletion, leading to different LDB ages, as shown in Table 2. For spots, we used the spot models from Somers et al. (2019, 2020).

We list the resulting age bounds from each model in Table 2. The age ranges from each model are broadly consistent, with lower age bounds ranging from 23–26 Myr, and upper age bounds from 28–32 Myr. The largest age discrepancies come from using the SPOT models with spot fractions >50%. While individual stars may have large spot fractions (Gully-Santiago et al. 2017), we expect the bulk of the stars here to have spot fractions $\lesssim$30% (Savanov et al. 2018; Cao et al. 2022; Klein et al. 2022). Thus, we include the ages from the SPOT model of only 17% and 34% in the table, both of which are consistent with the ages from the other models tested.

We take 27 ± 3 Myr as the age of the association to encompass all of these estimates.

A number of effects could cause Li-poor stars to appear above the LDB or vice versa. Unresolved binary stars that are Li-rich could appear to be as much as 0.75 mag brighter than the individual components, raising them on the CMD to look younger. Baraffe & Chabrier (2010) suggested that cold, episodic accretion onto young low-mass stars could cause early Li depletion in individual stars, leading a star to look older, but Sergison et al. (2013) found no evidence for this in two young associations, and it should not impact the age estimates here because we have multiple reliable detections. Poor parallaxes (e.g., on binaries), and stellar variability may also affect the CMD position at the $\lesssim$0.1 mag level, which can explain some of the spread.

Likely the largest cause of anomalous stars is nonmember interlopers, either younger interlopers from the nearby LCC populations or older interlopers from the field. A possible example of this is the star TIC 443273186, which is the lowest-luminosity star we observed at $M_K = 6.9$, but has no significant Li detection. This star has a low CMD position compared to other association candidate members, and is likely a field interloper rather than an association member.

While the LDB in low-mass stars is the most accurate method of using Li measurements to determine association age, it is also possible to estimate an association's age by examining the full sequence of Li abundance as a function of color (see Soderblom et al. 2014, for a review). Because this method uses Li abundance, rather than the simple threshold used by the LDB, and requires conversion between modeled A(Li) and measured EW(Li), it is more model-dependent than the LDB method, but serves here as an additional check on the association age.

First, we compare the magnetic DSEP stellar evolution models (Feiden 2016) against the Li measurements of MELANGE-4 M-dwarf members, shown in the left panel of Figure 7. We convert EW(Li) to Li/Li$_0$ by dividing each by the predicted initial EW(Li) for M dwarfs from (Zapatero Osorio et al. 2002; 700 mÅ). The measured values lie between the models for a 20 and 30 Myr association. Next, we compare the Li sequence of MELANGE-4 against that of three benchmark associations with ages ranging from 3–40 Myr. We supplement our EW(Li) measurements of MELANGE-4 members (see Section 3.3 and Table 6) with literature measurements for five higher-mass stars, taken from Mamajek et al. (2002),

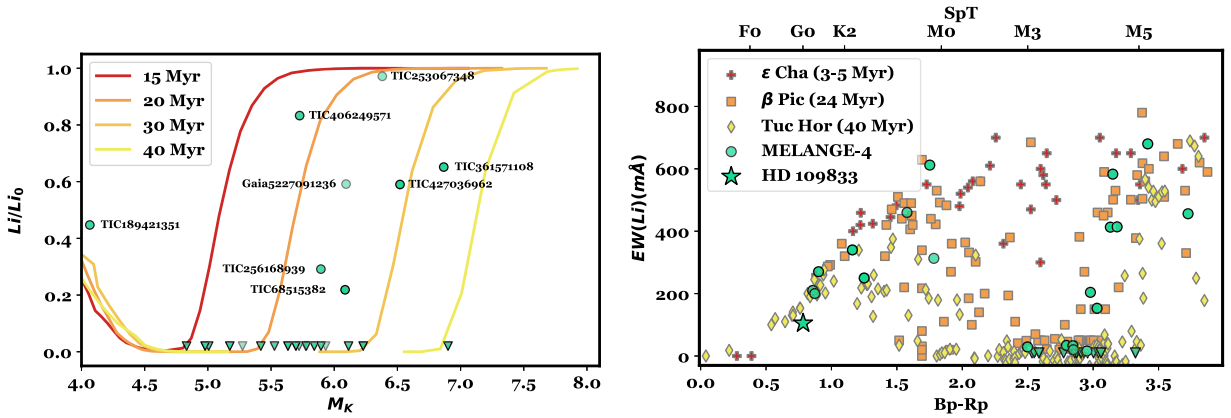

Figure 7. Lithium measurements for MELANGE-4. (Left) Fraction of initial Li abundance as a function of absolute K magnitude, overplotted with DSEP magnetic isochrones (Feiden 2016). EWs of association members were converted to $\mathrm{Li}/\mathrm{Li}_0$ using the curve of growth from Zapatero Osorio et al. (2002). The transparency of the points corresponds to their kinetic membership probability from BANYAN Σ, such that the most likely interlopers are the faintest. (Right) Comparison of MELANGE-4 Li sequence and Li sequences of known associations. For members of each association, Li EWs are shown as a function of Gaia $Bp - Rp$. EWs of MELANGE-4 members marked with downward triangles are upper limits. The transparency of the points corresponds to their kinetic membership probability from BANYAN Σ, such that the most likely interlopers are the faintest. Li measurements of MELANGE-4 members are supplemented with an additional five measurements from Mamajek et al. (2002), Torres et al. (2006), and Pecaut & Mamajek (2016). The Li measurements of β Pic members are taken from Shkolnik et al. (2017), measurements of ϵ Chamaeleontis members from Murphy et al. (2013), and measurements for Tuc-Hor from da Silva et al. (2009) and Kraus et al. (2014).

Table 2
Upper and Lower Age Bounds Given by Each of the Models Used

Model	Lower Bound	Upper Bound
BHAC15	24 Myr	28 Myr
DSEP (GS98)	23 Myr	29 Myr
DSEP Mag (GS98)	24 Myr	30 Myr
DSEP Mag (AGSS09)	26 Myr	32 Myr
SPOT (17%)	23 Myr	31 Myr
SPOT (34%)	24 Myr	31 Myr

Note. The upper bound corresponds to the age given an LDB at the magnitude of the faintest observed star without Li, and the lower bound corresponds to the age given an LDB at the magnitude of the brightest observed stars with Li.

Torres et al. (2006), and Pecaut & Mamajek (2016). The Li sequence of MELANGE-4 lies on top of that of the 24 Myr old β Pic association, shown in orange in the right panel of Figure 7. The association has more Li at $B_P - R_P \simeq 3.0$ than the older Tuc-Hor association (40 Myr), and lower Li (more depletion) at $1.7 < B_P - R_P < 3.0$ when compared to the younger 3–5 Myr ϵ Chamaeleontis association. Both of these tests support our measured LDB age of 27 ± 3 Myr.

4.4. Age from Isochrones

We independently estimate the age of MELANGE-4 by comparing the CMD to solar-metallicity isochrones using a Gaussian mixture model. For this analysis, we use the solar-metallicity PARSEC (v1.2S) models (Bressan et al. 2012) rather than one of the models used in the lithium analysis (Section 4.3), as those models do not reach the highest mass association members critical for differentiating between ages. Following Mann et al. (2022), we use a mixture model,[36] based on the method outlined in Hogg et al. (2010) and a Markov Chain Monte Carlo (MCMC) framework with `emcee` (Foreman-Mackey et al. 2017). The basic method is to fit the population with the combination of two models, one describing the single-star sequence of members, and one describing everything else (outliers). The second population may itself contain multiple populations, such as binaries, field interlopers, and young stars in Sco-Cen but not part of MELANGE-4.

The fit has six free parameters (units in brackets): the association age (τ [myr]), the average reddening across the association ($E(B-V)$ [mags]), the amplitude of the outlier population (P_B), the offset of the outlier population from the main population CMD (Y_B [mags]), the variance of the outliers around the mean (V_B [mags]), and a term to capture missing uncertainties or differential reddening across the association (f [mags]). All parameters evolve under uniform priors bounded by physical barriers, although $E(B-V)$ is allowed to go negative to avoid Lucy-Sweeney bias. We re-sample the isochrone grid to ensure uniform sampling in age. We run the MCMC with 50 walkers until it passed at least 50 times the autocorrelation time after a burn-in of 5000 steps (a total of 30,000 steps).

We perform the comparison using Gaia photometry and parallaxes for the final membership list described in Section 2.4. While the mixture model can handle outliers, it can be sensitive to multiple kinds of outliers as we expect here (binaries, LCC members, field stars, targets with poor parallaxes or photometry). So we remove stars with RUWE >1.4 (likely to be binaries; Ziegler et al. 2019; Wood et al. 2021), stars with $\mathrm{S/N} < 30$ in their parallax or any photometry, and any target outside the range of our model grid. This reduces the list of stars to 219.

As we show in Figure 8, the isochrone fits the sequence relatively well. One region of disagreement is the under-luminous G dwarfs around $B_P - R_P \simeq 0.9$, which includes HD 109833. At 20–30 Myr, this part of the CMD corresponds to stars' transition into He-3 burning, which leads to a rapid drop in the brightness of the star during the transition period. The resulting bend in the CMD is seen in the models as well as the similarly aged β Pic (Mamajek & Bell 2014). The fit is marginally consistent with the observations of HD 109833, but the three stars redward look like main-sequence interlopers. HD 109833's CMD position is an excellent match to the 30 Myr (and older) isochrones, so the discrepancy may be due to a modest (2–3 Myr) age spread, or other systematics in the

[36] https://github.com/awmann/mixtureages

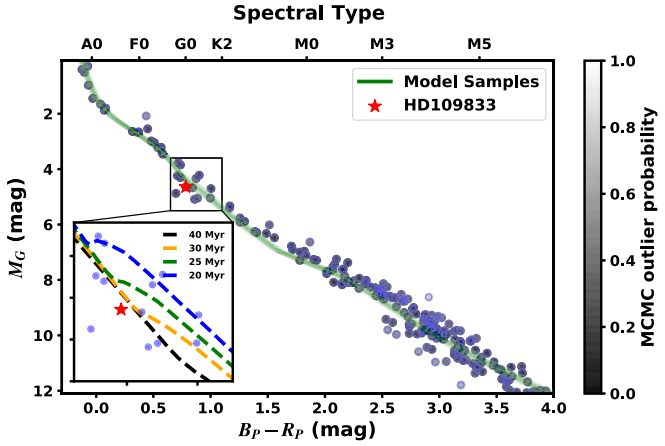

Figure 8. Comparison of the PARSEC isochrones to high-probability members of MELANGE-4 (circles). Stars are shaded by their outlier probability, as determined by the mixture model fit. Outliers are not necessarily nonmembers. The red star shows the planet host (HD 109833). The green lines are 100 random draws from the MCMC using the PARSEC isochrones and fit reddening. The inset shows the region around HD 109833 and representative-age model predictions.

models. Another possibility is that HD 109833 is a young field interloper, which we discuss further in Section 8.

The best-fit age from our fit is 26.0 ± 2.1 Myr. Repeating the analysis with DSEP (Dotter et al. 2008) with magnetic enhancement (Feiden 2016) yields a consistent but slightly older age of 27.1 ± 2.3 Myr. We use the age from the PARSEC fit because the DSEP models did not include stars above $1.7 M_\odot$ at this age. These high-mass stars provide an age constraint independent of the LDB age (which relies on mid-M dwarfs).

Fitting the full population without the cuts above gives a younger age (23 ± 3 Myr). However, when using the full sample, the outlier model fits the main-sequence interlopers, treating binaries and LCC interlopers as part of the main population (both of which bias the fit to younger ages). Similar small adjustments to the fitting method, such as nonsolar composition, also change the resulting age at the $\simeq$2 Myr level, generally preferring older ages. This suggests that systematic errors are comparable to measurement errors. All ages are in excellent agreement with our 27 ± 3 Myr age from the LDB (Section 4.3).

5. Directly Imaged Planets in MELANGE-4

Along with the newly identified planet host HD 109833 (discussed in Sections 6 and 7), three other candidate members of MELANGE-4 host four planetary-mass objects previously identified through direct imaging surveys. These systems represent a nontrivial fraction of all of the directly imaged planetary-mass companions (Currie et al. 2022), so a change in their age (and hence derived masses) could impact population-level statistics.

To update the masses of the directly imaged planets, we analyze the reported luminosity or absolute magnitude in the original papers and compare them to the weak-nonequilibrium ATMO2020 models of Phillips et al. (2020) using linear interpolation. We first verify that when using the originally asserted ages, we recover consistent masses, so any difference is primarily a result of the revised (older) age.

5.1. TYC 8998-760-1 (YSES 1)

TYC 8998-760-1 is a young K-dwarf type star with two directly imaged, wide companions from the Young Suns Exoplanet Survey (YSES) direct imaging survey (Bohn et al. 2020a, 2020b). The star has been classified as a $\simeq$16 Myr old member of LCC (e.g., Pecaut & Mamajek 2016). However, using our updated BANYAN Σ parameters, we find that it is a high-probability candidate member of MELANGE-4. The star's position, proper motions, and velocity are near the center of MELANGE-4, with a BANYAN Σ membership probability of 99.1%.

Assuming an age of 16.7 ± 1.4 Myr, Bohn et al. (2020a, 2020b) measured masses of $14 \pm 3 M_{\rm Jup}$ and $6 \pm 1 M_{\rm Jup}$ for planets YSES-1 b and YSES-1 c, respectively. Using the age of MELANGE-4 (27 ± 3 Myr; see Section 4), we estimate masses of $21.8 \pm 3 M_{\rm Jup}$, and $7.2 \pm 0.7 M_{\rm Jup}$. As expected, the new masses are much larger than the earlier values, although still ($<3\sigma$) consistent due to large uncertainties on the nearly vertical evolution of late-type pre-MS stars and brown dwarfs.

5.2. TYC 8984-2245-1 (YSES 2)

Like TYC 8998-760-1, TYC 8984-2245-1 is a young K-dwarf with a directly imaged companion observed by the YSES survey (Bohn et al. 2021). Several surveys of LCC have previously included TYC 8984-2245-1 as a member (e.g., Preibisch & Mamajek 2008; Gagné et al. 2018). However, using the Gaia DR3 RV of 12.93km s^{-1}, we find that it is a better match for MELANGE-4, with a kinematic membership probability of 94.8%.

We re-estimate the mass of YSES-2 b using the H and K magnitudes and find a new mass of $8.4 \pm 1.5 M_{\rm Jup}$. Again, this is a higher mass but still consistent with the prior estimate of $6.3^{+1.3}_{-0.9} M_{\rm Jup}$ (Bohn et al. 2021).

5.3. HD 95086

HD 95086 is an A8 pre-MS star, with both a directly imaged planet and an imaged debris disk (Moór et al. 2013; Rameau et al. 2013). de Zeeuw et al. (1999) and Rizzuto et al. (2011) both considered it to be a member of the LCC population, but Booth et al. (2021) argued that HD 95086 is instead a member of Carina, simultaneously proposing a younger (17 Myr) age for Carina.

The RV of HD 95086 has been measured multiple times by different sources; all of them strongly favor membership in MELANGE-4. Madsen et al. (2002) estimated an astrometric RV of 10.1 ± 1.2 km s^{-1}, which gives a BANYAN Σ membership probability of 98.7% for MELANGE-4, a 1.3% probability of being a field star, and $<1e-4$% for any of the LCC groups or Carina. Moór et al. (2013) measured $RV = 17 \pm 2$ km s^{-1}, with which the probability of membership in MELANGE-4 increases to 99.1%, with a probability of 0.66% for Carina and $<1e-4$% for all of the LCC groups. The Gaia DR3 velocity is a similar $RV = 18.04 \pm 0.16$ km s^{-1}, which gives a membership probability of 98.9% for MELANGE-4, 0.77% for membership in Carina, and 0.30% for field.

Using the previously assumed age of 17 ± 2 Myr, De Rosa et al. (2016) derived a mass of $4.4 \pm 0.8 M_{\rm Jup}$, placing HD 95086b among the least-massive planets yet detected with direct imaging. Using the K-band luminosity and the new, older age, we estimate a higher mass of $7.2 \pm 0.7 M_{\rm Jup}$. This shows more tension with the discovery value than for the other

Table 3
Properties of the Host Star HD 109833

Parameter	Value	Source
	Identifiers	
HD	109833	
HIP	61723	Hipparcos
TOI	1097	Guerrero et al. (2021)
Gaia	5838450865699668736	Gaia DR3
TIC	360630575	Stassun et al. (2018)
2MASS	J12390642-7434263	2MASS
	Astrometry	
α	189.775832	Gaia DR3
δ	−74.574021	Gaia DR3
μ_α (mas yr^{-1})	-50.489 ± 0.012	Gaia DR3
μ_δ (mas yr^{-1})	-6.764 ± 0.014	Gaia DR3
π (mas)	12.5686 ± 0.0118	Gaia DR3
	Photometry	
$G_{\rm Gaia}$ (mag)	9.145 ± 0.003	Gaia DR3
$\rm BP_{Gaia}$ (mag)	9.451 ± 0.006	Gaia DR3
$\rm RP_{Gaia}$ (mag)	8.668 ± 0.004	Gaia DR3
B_T (mag)	10.082 ± 0.027	Tycho-2
V_T (mag)	9.380 ± 0.020	Tycho-2
J (mag)	8.144 ± 0.023	2MASS
H (mag)	7.890 ± 0.038	2MASS
Ks (mag)	7.820 ± 0.026	2MASS
W1 (mag)	7.772 ± 0.028	ALLWISE
W2 (mag)	7.814 ± 0.020	ALLWISE
W3 (mag)	7.787 ± 0.018	ALLWISE
	Kinematics & Position	
$\rm RV_{Bary}$ (km s^{-1})	10.73 ± 0.23	Gaia DR3
X (pc)	41.39 ± 0.04	This work
Y (pc)	-66.00 ± 0.06	This work
Z (pc)	-16.16 ± 0.02	This work
U (km s^{-1})	-10.84 ± 0.30	This work
V (km s^{-1})	-18.3 ± 0.48	This work
W (km s^{-1})	-5.58 ± 0.12	This work
	Physical Properties	
$P_{\rm rot}$ (days)	5.111 ± 0.51	This work
$v \sin i_*$(km s^{-1})	10.5 ± 0.2	This work
i_* (°)	>84	This work
$F_{\rm bol}$(erg cm^{-2} s^{-1})	$(6 \pm 0.4) \times 10^{-9}$	This work
$T_{\rm eff}$ (K)	5881 ± 50	This work
log g(dex)	4.45 ± 0.10	This work
$M_\star$ ($M_\odot$)	1.08 ± 0.05	This work
$R_\star$ ($R_\odot$)	1.00 ± 0.04	This work
$L_\star$ ($L_\odot$)	1.18 ± 0.08	This work
[M/H]	-0.07 ± 0.08	This work
$\rho_\star$ ($\rho_\odot$)	1.08 ± 0.17	This work
Age (Myr)	27 ± 3	This work

three planets, but the new value is still marginally consistent with the original (2.6σ).

6. Parameters of TOI-1097

We summarize constraints on the candidate-planet host star in Table 3, the details of which we provide in this section.

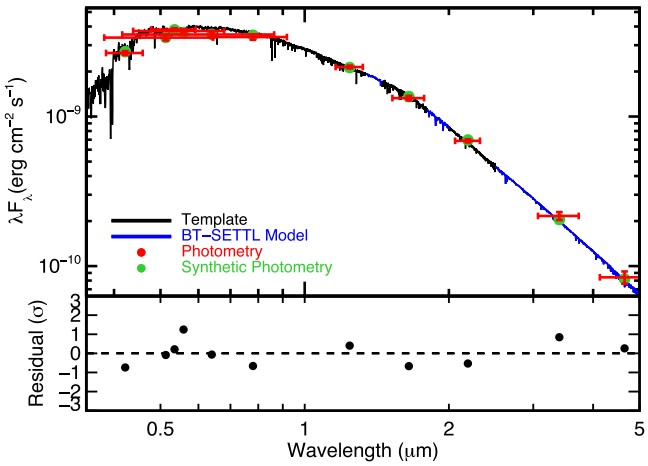

Figure 9. Best-fit template spectrum (G1V; black) and synthetic photometry (green) compared to the observed photometry of HD 109833 (red). Errors on observed photometry are shown as vertical errors, while horizontal errors indicate the approximate width of the filter. BT-SETTL models (blue) were used to fill in regions of high telluric absorption or beyond the template range. The bottom panel shows the photometric residual in units of standard deviations.

6.1. Fit to the Spectral Energy Distribution

To determine $T_{\rm eff}$, R_*, and L_* of HD 109833, we fit the spectral energy distribution (SED) following the methodology from Mann et al. (2016b). To summarize, we compare the observed photometry to a grid of optical and near-IR spectra of nearby unreddened stars. Most spectra are drawn from Rayner et al. (2009), supplemented by Hubble's Next Generation Spectral Library (Heap & Lindler 2016). To fill in gaps in the spectrum, we use BT-SETTL CIFIST atmospheric models (Baraffe et al. 2015), fitting to the template spectrum as outlined in Gaidos & Mann (2014). This also provides an estimate of $T_{\rm eff}$. We integrate the resulting full SED to determine the bolometric flux ($F_{\rm bol}$), which combined with the Gaia DR3 parallax, gives us the total luminosity (L_*). We then use the Stefan-Boltzmann relation to calculate R_* from $T_{\rm eff}$ and L_*.

For our fit, we use photometry from Tycho-2 (Høg et al. 2000), 2MASS (Skrutskie et al. 2006, 2003), the Wide-field Infrared Survey Explorer (Wright et al. 2010, 2019), and Gaia DR3 (Gaia Collaboration et al. 2021). We exclude W3 and W4 photometry in our fit because the star's young age allows for the possibility of a cool debris disk. To account for variability in the star, we add 0.02 mags in quadrature to the errors of all optical photometry. In total, the fit includes six free parameters: the choice of template, A_V, three parameters that describe the atmospheric model selection (log g, $T_{\rm eff}$, and [M/H]), and a scale factor between the model and the photometry (S).

The resulting fit, shown in Figure 9, gives $T_{\rm eff} = 5950 \pm 90$ K, $F_{\rm bol} = (6.0 \pm 0.4) \times 10^{-9}$ (erg cm^{-2} s^{-1}), $L_* = 1.18 \pm 0.08 L_\odot$, $R_* = 1.00 \pm 0.04 R_\odot$, and a spectral type of G1V–G3V. The best-fit model predicts a W3 that is lower than the observed value by 10%–20%, which suggests the presence of a debris disk. However, the excess is below significance for some templates, and no significant excess is seen in the less-precise W4 point.

6.2. Fit to the High-resolution Spectra

In addition to the SED fit described above, we derive the atmospheric parameters from both the CHIRON and HARPS spectra. These served as an independent test of $T_{\rm eff}$, while also providing constraints on metallicity, $\log g$, and rotational broadening ($v \sin i_*$).

We derive spectral parameters ($T_{\rm eff}$, $\log g$, $v \sin i_*$, and [M/H]) from the CHIRON spectra of HD 109833 using the Spectral Parameter Classification (SPC) tool (Buchhave et al. 2012). SPC cross-correlates the observed spectrum against a grid of Kurucz atmospheric models (Kurucz 1993b). Four parameters are allowed to vary: $T_{\rm eff}$, $\log g$, bulk metallicity ([M/H]), and $v \sin i_*$. We run each spectrum separately, then combine the results, yielding $T_{\rm eff} = 5881 \pm 45$ K, $\log g = 4.445 \pm 0.041$, $[{\rm M/H}] = -0.068 \pm 0.053$, and $v \sin i_\star = 10.5 \pm 0.2 {\rm km\,s^{-1}}$. The assigned errors reflect the scatter between spectra, and do not include systematic errors. Based on comparison with benchmark stars (e.g., asteroseismic targets), we adopt error floors of 50 K, 0.1 dex in $\log g$, and 0.08 dex in [M/H]. Even with the error floors, the resulting $T_{\rm eff}$ estimate is more precise than those from our SED fit.

We separately derive spectral parameters from the HARPS spectra using the methodology described in Sousa (2014) and Santos et al. (2013). We first measure the EWs of 224 FeI and 35 FeII lines using the ARES v2 code[37] (Sousa et al. 2015). Then we use these EWs together with a grid of Kurucz model atmospheres (Kurucz 1993a) and the radiative transfer code MOOG (Sneden 1973) to determine the parameters under the assumption of ionization and excitation equilibrium. The abundances of Mg and Si are also derived using the same tools and models as detailed in, e.g., Adibekyan et al. (2012, 2015). Although the EWs of the spectral lines are automatically measured with ARES, we performed a careful visual inspection of the EWs measurements, as only three lines are available for the Mg abundance determination. This analysis gives us $T_{\rm eff} = 5975 \pm 70$ K, $\log g = 4.58 \pm 0.11$, $[{\rm Fe/H}] = 0.08 \pm 0.05$, $[{\rm Mg/H}] = 0.02 \pm 0.06$, and $[{\rm Si/H}] = 0.05 \pm 0.05$.

The rotational projected velocity ($v \sin i_* = 9.9 \pm 0.8$ km s^{-1}) is derived from the HARPS spectra by performing spectral synthesis with MOOG on 36 iron isolated lines and by fixing all of the stellar parameters, macroturbulent velocity, and limb-darkening coefficient (Costa Silva et al. 2020). The limb-darkening coefficient (0.58) is determined using the stellar parameters as described in Espinoza & Jordán (2015) assuming a linear limb-darkening law. The macroturbulent velocity (3.6 km s^{-1}) is determined using the temperature and gravity-dependent empirical formula from Doyle et al. (2014).

Despite using different methods and data, the two sets of results above are all consistent within 2σ, and both are consistent with our SED analysis. We use the CHIRON/SPC fit for $T_{\rm eff}$ and $v \sin i_*$, and the abundances from the HARPS/MOOG analysis. Using any set, or the average of the three, does not significantly change any results or conclusions of the paper.

6.3. Mass from Stellar Isochrones

To determine the stellar mass (M_*), we compare the observed photometry (from Gaia G, B_P, R_P; 2MASS J, H, K; and Tycho B_T, V_T) to predictions from the DSEP magnetic models (Feiden 2016). The DSEP magnetic model covers ages from 1 Myr−10 Gyr and masses between $0.09\,M_\odot$ and $2.45\,M_\odot$. To explore systematics between models, we also run a fit using the PARSEC (v1.2S) models (Bressan et al. 2012). We apply the comparison within an MCMC framework with `emcee`, simultaneously fitting for four parameters: age, M_*, A_V, and a factor describing the underestimation of the errors on the measured photometry (f). For both grids, we assume solar metallicity.

To alleviate the computational cost of bilinearly interpolating the model grid at every step, we pre-interpolate the grid using the `isochrones` package (Morton 2015) to give it tighter spacing in age and mass (0.1 Myr and $0.01\,M_\odot$) than expected errors. Grid re-sampling also lets us enforce uniform sampling in age. During each sampling step, the procedure is as follows: first, we employ a hybrid interpolation method, which finds the nearest neighbor in age, then linearly interpolates in mass, to extract predicted photometry and stellar parameters (such as $T_{\rm eff}$ and R_*). Second, the predicted photometry is corrected according to the given A_V value, using a combination of `synphot` (Lim 2020) and the extinction model presented by Cardelli et al. (1989). Lastly, we compare the corrected model photometry to the measured photometry in a Bayesian maximum-likelihood framework.

We place Gaussian priors of 27 ± 3 Myr on age and 5881 ± 50 K on $T_{\rm eff}$, following our analysis of the spectrum. All other fit parameters evolve under uniform priors. For the DSEP magnetic model, we find age $= 34.5 \pm 1.7$ Myr and $M_* = 1.13 \pm 0.02\,M_\odot$, while PARSEC gives age $= 30.9 \pm 0.8$ Myr and $M_* = 1.03 \pm 0.02 M_\odot$. The errors are statistical only, as is evident by the $\simeq 3\sigma$ disagreement on M_* ($0.10 \pm 0.03\,M_\odot$) between the two methods. We adopt $M_* = 1.08 \pm 0.05 M_\odot$, which encompasses both values and more accurately reflects the systematic limits of the models (Tayar et al. 2022).

6.4. Stellar Inclination

We use the combination of $v \sin i_*$, $P_{\rm rot}$, and R_* to estimate the stellar inclination (i_*). Since the transiting planets are nearly edge-on ($i > 85°$; Section 7), this measures the alignment between the stellar spin and planetary orbit axes. Simplistically, the equatorial velocity (V) in $v \sin i_*$ can be derived straightforwardly using $V = 2\pi R_*/P_{\rm rot}$. In practice, however, this calculation requires additional corrections due to the effects of sky-projection and measurement uncertainties, which could cause the appearance of $v \sin i_* > V$. We followed the formalism from Masuda & Winn (2020). Using either $v \sin i_*$ determined in Section 6.2 gave an inclination consistent with edge-on. The CHIRON $v \sin i_*$ gave a limit of $i_* > 84°$ at 95% confidence, while the HARPS $v \sin i_*$ yielded $i_* > 66°$.

7. Parameters of TOI-1097 b and TOI-1097 c

7.1. Detection of the Planetary Signals

The first planet signal, TOI-1097.01, was originally detected from the joint search of sectors 11 and 12 as part of the Quick-Look Pipeline search (Huang et al. 2020). The candidate passed initial vetting and was alerted on 2021 October 29.

To confirm the detection and search for additional planets, we use the Notch and LoCoR pipelines described in Rizzuto et al. (2017).[38] To briefly summarize, the Notch filter fits a

[37] http://www.astro.up.pt/~sousasag/ares

[38] https://github.com/arizzuto/Notch_and_LOCoR

window of the light curve as a combination of an outlier-robust second-order polynomial and a trapezoidal notch. The window is shifted along the light curve until the variability is detrended (flattened) while preserving the planet signal. At each data point, Notch calculates the improvement from adding the trapezoidal notch based on the change in the Bayesian Information Criterion (BIC) compared to modeling just a polynomial.

After running Notch, we perform a box-least-squares search on the BIC values and recovered both the initial 9.2 day planet candidate from TESS and an additional signal at either 13.9 or 41 days (it was initially ambiguous). Additional short-cadence data from Sectors 38 and 39 made it clear that the shorter 13.9 day period was the correct one. This candidate was later recovered by a TESS SPOC pipeline joint search of sectors 38 and 39 (Jenkins 2002; Jenkins et al. 2010, 2020) and designated TOI-1097.02 on 2022 March 24 by the TESS Science Office.

There were no other significant detections from our Notch search, other than those near aliases of the planets and/or rotation period. The BIC is sensitive to single-transit detections (Rizzuto et al. 2020), but we did not identify any such signals that survived visual inspection.

7.2. MCMC Fit of Light Curves

To determine the planet parameters, we compare a transit model to the TESS photometry using the `MISTTBORN` (MCMC Interface for Synthesis of Transits, Tomography, Binaries, and Others of a Relevant Nature) code.[39] `MISTTBORN` uses `BATMAN` (Kreidberg 2015) to generate model light curves, `celerite` (Foreman-Mackey et al. 2017) to model the stellar variability, and `emcee` (Foreman-Mackey et al. 2013) to explore the parameter space. More details on the code can be found in Mann et al. (2016a) and Johnson et al. (2018).

The standard implementation of `MISTTBORN` fits for four parameters for each transiting planet: time of periastron (T_0), orbital period of the planet (P), planet-to-star radius ratio ($R_p/R_\star$), and impact parameter (b). It also fits for three parameters specific to the host star: stellar density ($\rho_\star$) and two limb-darkening parameters (q_1, q_2) using the triangular sampling prescription from Kipping (2013).

Stellar variability from the star was far stronger than the transit signal over all TESS data. We fit the variations using the Gaussian Process (GP) feature within `MISTTBORN`. We initially adopted the GP kernel based on a mixture of two simple harmonic oscillators but found that the parameters associated with the second oscillator were unconstrained and never fully converged. Instead, we adopt a single-term simple harmonic oscillator, based on the model used by Foreman-Mackey et al. (2017), which includes three GP terms: the period ($\ln(P_{\rm GP})$), amplitude (lnAmp), and the decay timescale for the variability (quality factor, $\ln Q$).

Although eccentricities of young planets are expected to be near zero due to gravitational interactions and drag from the circumstellar disk (Tanaka & Ward 2004), this young regime has few observational constraints. So, we run two fits, one with eccentricity locked at zero and a uniform prior on $\rho_\star$, and a second fitting two parameters describing eccentricity and argument of periastron ($\sqrt{e}*\cos(\omega)$, and $\sqrt{e}*\sin(\omega)$) with a uniform prior, and assuming a Gaussian prior for $\rho_\star$ drawn from Section 6.

We apply Gaussian priors on the limb-darkening coefficients based on the values from the `LDTK` toolkit (Parviainen & Aigrain 2015), with errors accounting for the difference between these two estimates (which differ by 0.04−0.08).

After an initial fit, we find a few walkers wandered off the transit signal, adjusting the GP signal to partially fit the transit. To prevent this, we place weak Gaussian priors on T_0, P, and $\ln(P_{\rm GP})$ around the initially estimated values from a least-squares fit, and with widths of 0.1 day, 0.1 day, and 0.1 dex (1 day), respectively. The width of these priors was much larger than the final uncertainties and had a negligible effect on the result (other than preventing the wandering walkers). All other parameters evolve under uniform priors with physically motivated limits.

For the first fit (e locked at 0), we run the MCMC using 50 walkers for 100,000 steps including a burn-in of 20,000 steps. This setup is sufficient for convergence based on the autocorrelation time. For the second fit, which has a lower acceptance fraction, we use 200 walkers and 100,000 steps (the same burn-in).

Both of the fits were broadly consistent, producing consistent q_1, q_2, and GP fit for the star, T_0, P, and R_P/R_* for both planets, and impact parameter for the outer planet. The impact parameter of the inner planet is higher when allowing nonzero eccentricities, but consistent within the uncertainties. The GP fit found a stellar rotation period of $P_{\rm GP} = 5.64 \pm 1.08$ days, consistent with the rotation period found using a Lomb-Scargle periodigram analysis, $P_{\rm rot} = 5.11 \pm 0.51$ days (see Section 3.1.2). Individual light curves for all four sectors and the GP fits are shown in Figure 10, and the resulting folded lightcurves and transit fits in Figure 11. MISTTBORN transit fit results are shown as corner plots in Figure 12, and listed in Table 4. The eccentric fit cannot rule out a zero eccentricity for either planet but does suggest a potentially eccentric orbit, especially for the outer planet, which has a best-fit eccentricity $e_c = 0.3^{+0.21}_{-0.19}$. The posterior distribution of eccentricity for each planet is shown in Figure 13.

7.3. False-positive Analysis

For our false-positive analysis, we first calculate the magnitude limit (Δm) of a potential blended source (bound or background) that could reproduce the transit signal, using the source brightness constraints described by Seager & Mallén-Ornelas (2003) and Vanderburg et al. (2019). This depends on the ingress or egress duration compared to the transit duration and reflects the true radius ratio, independent of whether there is contaminating flux:

$$\Delta m \leqslant 2.5 \log_{10}\left(\frac{T_{12}^2}{T_{13}^2 \delta}\right).$$

Here, δ is the transit depth, T_{12} is the ingress/egress duration, and T_{13} is the time between the first and third contact. We calculate Δm for the posterior samples for our floating eccentricity transit fit and take the 99.7% confidence limit. We find $\Delta m < 3.5$ and <5.3 for HD 109833 b and HD 109833 c, respectively.

Based on these magnitude limits, only two stars detected by Gaia (including HD 109833) could reproduce the transits of HD 109833 b, and three stars could reproduce HD 109833 c

[39] https://github.com/captain-exoplanet/misttborn

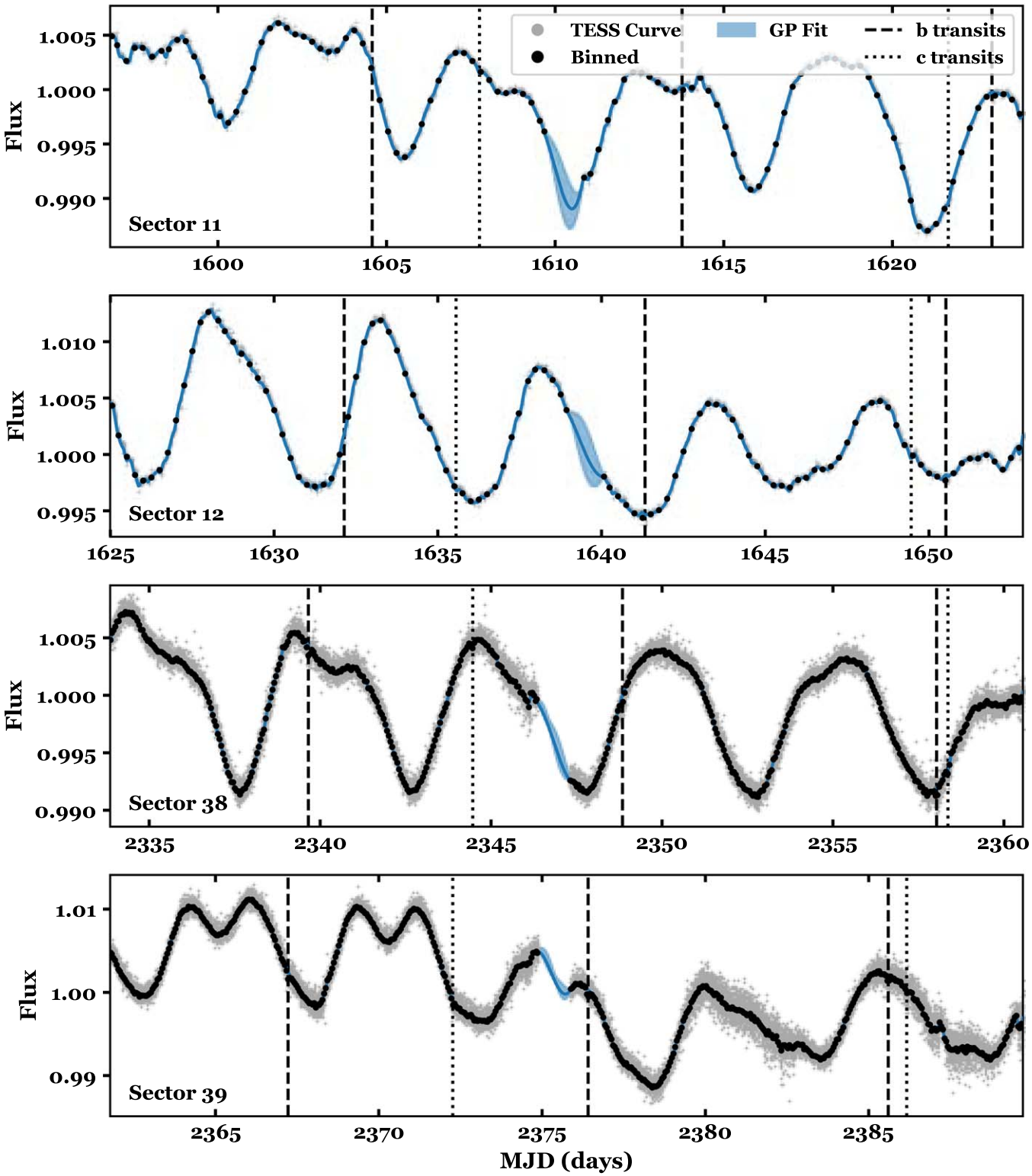

Figure 10. TESS light curves for Sectors (from top to bottom) 11, 12, 38, and 39. Data for each sector is shown as gray dots, and binned values are shown as black dots. The blue line indicates the model GP fit to the data with uncertainties (shaded region). The times of the transits are marked with dashed and dotted vertical lines for planets (b) and (c), respectively.

(see Figure 14). By selectively resizing the aperture, we rule out all stars other than HD 109833 as the source of the planetary signals. We also check this using the `tpfplotter` tool from Aller et al. (2020), and find four faint stars within the aperture, all with $\Delta T > 5$.

Separately, the SPOC data validation (Twicken et al. 2018; Li et al. 2019) centroid offsets for Sectors 38–39 exclude all TICv8.2 objects capable of producing the observed transit depths other than the target star. As with the transit duration and depth constraints above, this confirms that the only

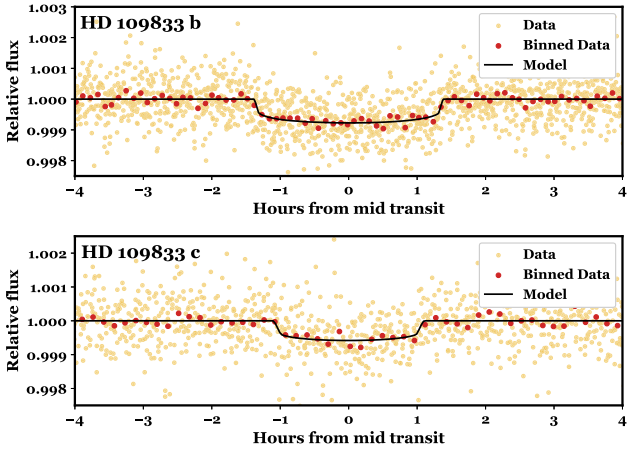

Figure 11. Phase-folded transits of HD 109833 b and HD 109833 c. The data are shown in yellow, with the 20 s cadence data from Sectors 38 and 39 binned to 2 m. Red points show all data binned together, and the black line shows the `batman` model using the results from the $e = 0$ `MISTTBORN` run.

remaining false-positive scenarios involve objects unresolved with HD 109833.

To handle unresolved sources, we use a combination of Multi Observational Limits on Unseen Stellar Companions (MOLUSC; Wood et al. 2021) and a tool for vetting and validating TESS Objects of Interest (Triceratops; Giacalone et al. 2021). `MOLUSC` provides limits on the range of possible companions allowed by the existing data, while `triceratops` combines the companion limits with information about the light curve to compute probabilities of given false-positive (FP) scenarios.

`MOLUSC` generates simulated companions and compares them to RV measurements, contrast imaging, and Gaia RUWE and imaging constraints. We test two different scenarios, one of a transiting stellar companion, for which the cosine of stellar inclination, $cos(i)$, is locked to only transiting companions, and one of any stellar companion, for which $cos(i)$ was drawn from a uniform distribution. In the second scenario, we assume the transits are caused by planetary-mass objects, but there is an additional stellar companion in the system. For both scenarios, we generate 5,000,000 companions, with orbital parameters drawn from realistic binary distributions (see Wood et al. 2021 for details). Across both scenarios, 91.3% of generated companions were ruled out. In the transiting scenario, we found 3σ detection limits of $\sim$0.4–0.7$M_{\rm Jup}$ at periods of 9−13 days. This alone rules out an eclipsing stellar companion (orbiting HD 109833) as the cause of the transit signals. As the planets are not detected in any of the included data sets, the mass limits do not include the planets. The nontransiting companion scenario, while allowing the possibility of a stellar companion at moderate periods, rules out nearly all companions with $M_{\rm comp} > 0.6M_{\odot}$ or $P < 100$ days.

To calculate the probability that each signal is due to a planet, we run `triceratops` using all four sectors of TESS data and the output binaries generated from `MOLUSC`. Including the `MOLUSC` output effectively limited the possible FP scenarios to those consistent with the observational limits. Of the 18 different scenarios considered by Giacalone et al. (2021), three are considered "true positives," i.e., the transiting planet, unresolved binary with a transiting planet around the primary, and unresolved background star with a transiting planet around the primary. By default, `triceratops` considers signals that come from a bound companion as false positives, even if the signal is still a transiting planet. We consider cases including a planet and a bound companion as true positives, as the signal was still from a young planet even if the radii are likely significantly underestimated.

For each planet, we run `triceratops` 20 times and find the mean and standard deviation of the false-positive probability (FPP). For HD 109833 b, we find FPP < 0.0003 (0.03%), with an additional $\simeq$1% probability that the planet orbits a bound companion. If HD 109833 b is orbiting a secondary companion with the predicted mass of $\sim 0.8M_{\rm Sun}$, it would still have a radius consistent with a planet.

For HD 109833 c, `triceratops` yielded a higher FPP of $9.2\% \pm 2.5\%$. Multiplanet systems are less likely to be false positives (e.g., Lissauer et al. 2012). Guerrero et al. (2021) recalculated this "multiplicity boost" for TOIs, i.e., the multiplicative factor that reflects the a priori probability that a candidate in a multitransiting system is a true positive. They estimate this to be $\simeq$50 for planets $R_p < 6R_{\oplus}$. Even the more conservative factor of 20 for all TOIs is still sufficient to bring HD 109833 c below the 1% required for validation.

8. Summary and Conclusions

In this paper, we present a new, 27 ± 3 Myr old association (MELANGE-4) on the outskirts of LCC. We initially identified the group from a population of pre-main-sequence M dwarfs comoving with a candidate transiting-planet host from TESS (TOI 1097). We gather a wide range of ground-based follow-up and archival data with the goals of (1) improving the list of likely members, (2) measuring the age and basic parameters of the association, (3) confirming the group is distinct from known young populations (Carina and LCC), and (4) validating and characterizing the planetary system TOI 1097.

We first perform a membership search for candidate members using an iterative process, resulting in list of 306 candidate members. A small number ($\lesssim$10) of the candidates sit unusually high or low on the CMD (see Figure 2) or have low lithium levels for their spectral type (see Figure 7). Thus, the list is not totally clean, but is still sufficient to estimate the age and properties of the group.

MELANGE-4's rotation, CMD, and lithium levels are consistent with an age of 25–30 Myr. Rotation provides only a qualitative check on the age (and membership) due to the large spread in rotation periods at this age (Rebull et al. 2018). A fit to the CMD with stellar models offers a consistent and arguably more precise age (26 ± 2 Myr), with an additional 2 Myr error based on differences between model grids and input assumptions. The most reliable age constraint comes from the lithium depletion, which provides an age of 27 ± 3 Myr that is almost entirely independent of model selection (see Table 2).

The association is kinematically close to LCC but is distinct in position, velocity, dispersion, and age. The LCC subpopulation that is closest in *XYZ* is most discrepant in velocity, and the group with the most similar velocity is farthest in *XYZ*. All of the known LCC subgroups are also significantly younger. In Section B, we analyzed all of the LCC subgroups using the same isochronal method we used for MELANGE-4 in Section 4.4, and found that the oldest LCC subgroup is 16.6 ± 1.1 Myr, inconsistent with our isochronal age (26 ± 2) and lithium-depletion age (27 ± 3 Myr) for MELANGE-4.

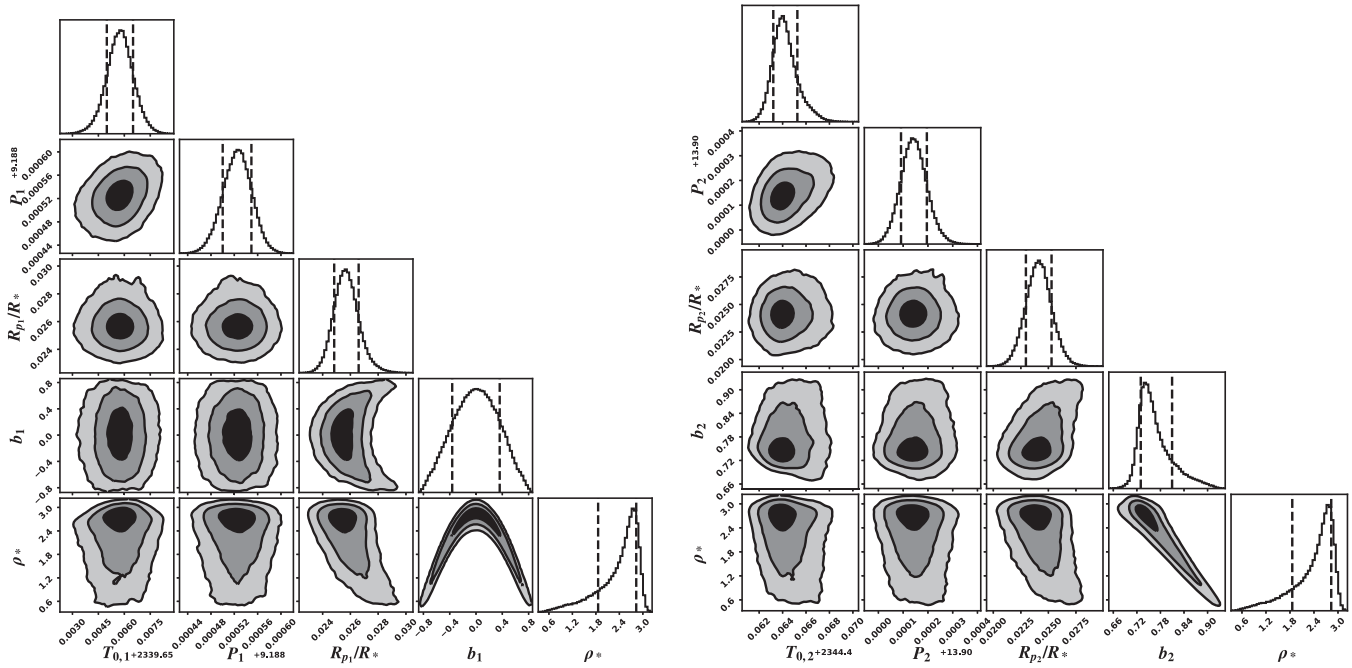

Figure 12. Corner plots of the MISTTBORN results for TOI-1097b (left) and TOI-1097c (right), with eccentricity locked to $e = 0$. Posterior distributions are shown as 2D contour plots, with levels corresponding to 1σ, 2σ, and 3σ, and as histograms with the 16th and 84th percentiles marked with dashed lines. Distributions are mostly Gaussian, with the exception of ρ_*, which has a long tail toward a less-massive stellar host. The distribution of ρ_* is shown on both plots, but only a single value is explored in the fit.

Of the other known moving groups in Gagné et al. (2018), the two closest in kinematics are Carina ($\Delta V \simeq 3.4$ km s^{-1}) and Columba ($\Delta V \simeq 4.1$ km s^{-1}). The cores of these groups are more than 30 pc from MELANGE-4 and are significantly older ($\simeq$45 Myr) than MELANGE-4. A more complicated possibility is that MELANGE-4 is a mix of members from Carina, Columba, and LCC. However, if this were the case, we would expect Li-rich low-mass stars to be preferentially closer to LCC and Li-poor ones close to Carina. We find instead that Li-rich PMS stars are spread throughout the association. We conclude that MELANGE-4 is distinct from any known young association.

We report the discovery of two transiting planets around the Sun-like star HD 109833, which we identify as a candidate member of MELANGE-4. The first planet was first identified by TESS, while the second planet was identified by our Notch analysis (and later by TESS). Both planets are super-Earth sized, with radii of $2.9R_E$ and $2.6R_E$, with periods of 9.2 and 13.9 days, close to a 3:2 resonance. We validate the b planet as planetary in nature. The c planet was a weaker detection and had an unusually short duration; `triceratops` gave a FPP of 10%. However, with the multiplicity boost, both planets meet the requirements for statistical validation.

Along with the newly discovered two-planet system around HD 109833 (this paper), three high-probability candidate members have directly imaged planetary-mass companions, TYC 8998-760-1, HD 95086, and TYC 8984-2245-1 (Rameau et al. 2013; Bohn et al. 2020a, 2021). These systems were previously placed in LCC or the Carina moving group, with assumed younger ages. Our older age changes the masses and inferred properties of the planets.

HD 109833 is *not* an unambiguous member of MELANGE-4. This is especially surprising since the planet host was the seed of our initial search that identified MELANGE-4. Most of our data favor membership. However HD 109833 has a lower CMD position than predicted for this age, and lies on the outskirts of the group in U and V velocity. As discussed in Section 4.4, this may be an issue with the models. While HD 109833 is clearly young (<200 Myr), the lithium levels are lower than expected for this age (Gutiérrez Albarrán et al. 2020) and compared to similar stars in the same association (Figure 7). The rotation period matches expectations for members of MELANGE-4, but is also consistent with ages up to 200 Myr. The strongest evidence in favor of membership is the 99.8% BANYAN Σ membership probability. We conclude that HD 109833 is likely part of MELANGE-4, but we cannot reject the possibility that it is a young field star coincidentally moving with MELANGE-4.

An older age for HD 109833 does not significantly impact our inferred properties of the star or planet. A star of this $T_{\rm eff}$ exhibits minimal change in CMD properties between hitting the main sequence ($\simeq$30 Myr) to the oldest ages consistent with Li and rotation (100–200 Myr), and our $T_{\rm eff}$ and R_* estimates did not make any assumptions about the age.

While the observed young-planet sample has grown dramatically in the last 5 yr (e.g., Mann et al. 2016b; David et al. 2016; Benatti et al. 2019; Newton et al. 2019), there are still few planets younger than 200 Myr, and very few known multiplanet systems of that age, so this discovery radically expands our sample of young planetary systems. Interestingly, both planets have radii comparable to field-age stars, while most of the young (<100 Myr) transiting planets land in the sub-Saturn desert (4–10 $R_\oplus$; Figure 15). This is less compelling if we adopt the older (100–200 Myr) age, but most planets at that age still appear inflated compared to their older counterparts (e.g., Newton et al. 2022).

The small size of the planets may be caused by photoevaporation of their atmospheres by high-energy radiation from the host star. However, comparison to the similar system V1298 Tau, a 23 Myr, multiplanet system in Group 29

Table 4
Parameters of HD 109833 b and HD 109833 c

Parameter	HD 109833 $e = 0$	HD 109833 e Float (Preferred)
Measured Parameters		
$\rho_\star$ ($\rho_\odot$)	$2.544^{+0.287}_{-0.714}$	$1.1027^{+0.1359}_{-0.1415}$
$q_{1,1}$	$0.303^{+0.101}_{-0.094}$	$0.321^{+0.141}_{-0.115}$
$q_{2,1}$	$0.364^{+0.077}_{-0.084}$	$0.325^{+0.109}_{-0.142}$
$\ln(P_{GP})$	$1.730^{+0.083}_{-0.081}$	$1.729^{+0.092}_{-0.081}$
$\ln(Amp)$	$-9.525^{+0.177}_{-0.164}$	$-9.531^{+0.183}_{-0.170}$
$\ln(Q)$	$0.618^{+0.035}_{-0.026}$	$0.618^{+0.036}_{-0.028}$
Parameter	HD 109833 b $e = 0$	e Float (Preferred)
Measured Parameters		
T_0 (BJD-2454833)	$1604.57376^{+0.00074}_{-0.00076}$	$1604.57374^{+0.00091}_{-0.00097}$
P (days)	$9.188525 \pm 2.5 \times 10^{-5}$	$9.188526 \pm 2.6 \times 10^{-5}$
$R_P/R_\star$	$0.02569^{+0.00091}_{-0.00085}$	$0.0265^{+0.0014}_{-0.0012}$
b	$0.25^{+0.25}_{-0.18}$	$0.61^{+0.15}_{-0.33}$
$\sqrt{e}\sin\omega$	...	$0.02^{+0.23}_{-0.25}$
$\sqrt{e}\cos\omega$	...	$-0.03^{+0.51}_{-0.46}$
Derived Parameters		
$a/R_\star$	$25.2^{+0.9}_{-3.0}$	$19.9^{+1.9}_{-2.1}$
i (°)	$89.4^{+0.4}_{-0.7}$	$88.13^{+1.0}_{-0.55}$
e	...	$0.18^{+0.24}_{-0.12}$
R_P ($R_\oplus$)	$2.802^{+0.099}_{-0.093}$	$2.888^{+0.152}_{-0.127}$
Parameter	HD 109833 c $e = 0$	e float (Preferred)
Measured Parameters		
T_0 (BJD-2454833)	$1607.75659^{+0.0012}_{-0.00092}$	$1607.7567^{+0.0015}_{-0.0011}$
P (days)	$13.900142 \pm 5.3 \times 10^{-5}$	$13.900148 \pm 5.7 \times 10^{-5}$
$R_P/R_\star$	$0.0241^{+0.0012}_{-0.0012}$	$0.0237^{+0.0018}_{-0.0016}$
b	$0.757^{+0.055}_{-0.027}$	$0.73^{+0.14}_{-0.32}$
$\sqrt{e}\sin\omega$	...	$0.2^{+0.24}_{-0.31}$
$\sqrt{e}\cos\omega$	...	$-0.0^{+0.54}_{-0.56}$
Derived Parameters		
$a/R_\star$	$33.2^{+1.2}_{-3.5}$	$29.4^{+4.5}_{-4.3}$
i (°)	$88.696^{+0.085}_{-0.3}$	$88.24^{+0.73}_{-0.34}$
e	...	$0.3^{+0.21}_{-0.19}$
R_P ($R_\oplus$)	$2.63^{+0.128}_{-0.125}$	$2.59^{+0.196}_{-0.175}$

Note. Results of the MISTBORN MCMC fitting of the planet transits.

David et al. (2019), shows that this may be unlikely. Poppenhaeger et al. (2021) find the X-ray luminosity, L_X, of V1298 Tau to be $L_X = 10^{30.1}$ erg s^{-1}. The X-ray luminosity of TOI 1097, calculated using the flux found by Freund et al. (2022), is comparatively lower, at $L_X = 10^{29.07}$. If photoevaporation is the driving factor of the planets' sizes, we would expect HD 109833, being of similar age, and having lower L_X, to have larger planets than V1298 Tau. However, V1298 Tau c and d, with periods of 8.25 and 12.40 days, respectively, have sizes $R_{P,c} = 5.59R_\oplus$, and $R_{P,d} = 6.41R_\oplus$, about twice the size of TOI 1097 b and c.

The orbital periods of the planets also fall near a 3:2 mean motion resonance, making this system one of only a few known young systems near resonance (e.g., Feinstein et al.

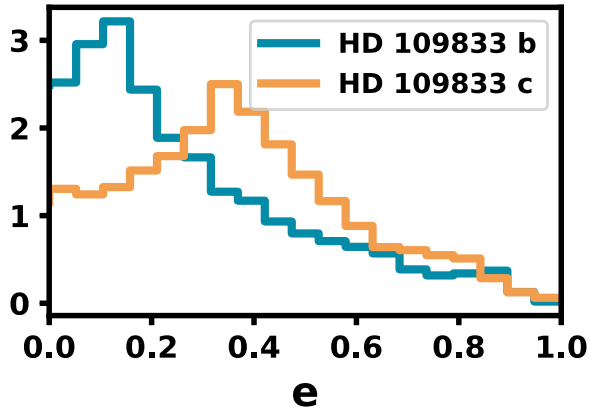

Figure 13. The posterior distribution of eccentricity resulting from the MISTTBORN fit, using a uniform prior distribution on e, and Gaussian prior on ρ_* from our stellar parameters. Both planets are consistent with zero eccentricity.

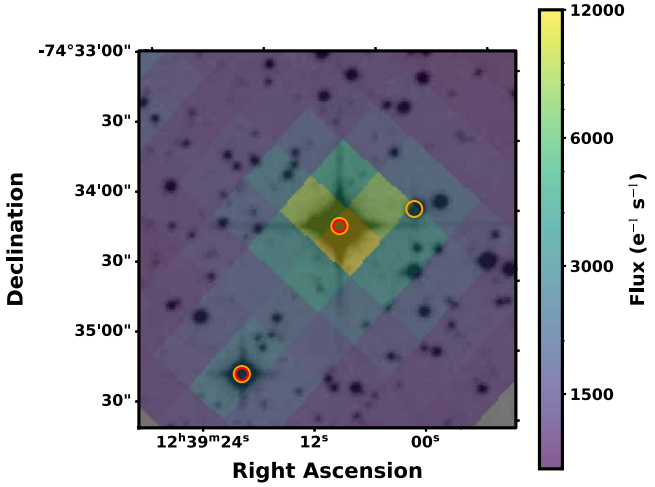

Figure 14. A TESS Sector 38 image colored by flux (see the color bar) on top of a DSS image (grayscale). Red circles indicate the two stars that could reproduce the transit signal for planet b, while orange indicates those that could reproduce c. The bright central star is HD 109833.

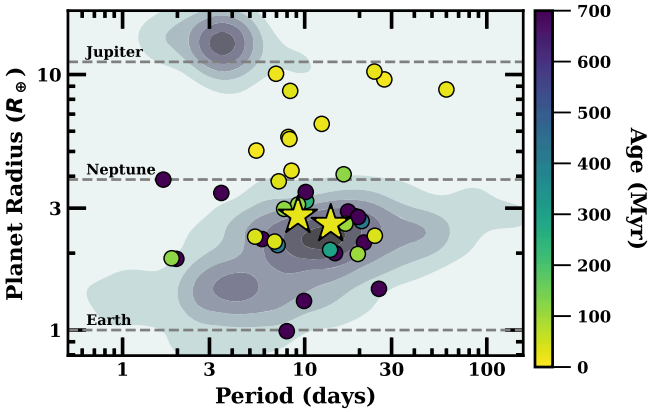

Figure 15. A comparison of the period–radius distribution of HD 109833 planets, other transiting planets from young associations (colored dots), and from the field (background contours). The young planets are colored according to their ages. Planets orbiting field stars are shown as density contours. HD 109833 b and HD 109833 c are shown as stars. Planet data is taken from Table 9 of Newton et al. (2022), with the addition of the young planets discovered by Zhou et al. (2022), Bouma et al. (2022), and Barber et al. (2022)

2022). The mechanism responsible for resonant chains is still unknown, and establishing the timescale in which they form is critical for understanding this process.

As a new and nearby association, with hundreds of candidate members, MELANGE-4 is an excellent subject for future observations and research. We do not expect that the membership presented here is either complete or contaminant-free, so additional studies on the membership and additional RV measurements are needed to better delineate the association members. Further observations of low-mass members to measure their Li abundance would improve the limits on the LDB age, which is currently limited by the small number of Li detections in the relevant mass range. New planet searches focusing on candidate members may find more $\sim$30 Myr planets within the association, further increasing the sample of young planets, while future studies on the relationship between MELANGE-4 and the nearby young associations could improve the understanding of the cloud collapse and star formation process.

The planet host, HD 109833, is also a promising subject for follow-up given its proximity to Earth and bright magnitude ($G = 9.14$). Additional observations may help to solidify its membership in MELANGE-4, or reject it as a member. Further characterization of the planets, including mass measurements and better constraints on eccentricity, may be possible with a search for transit timing variations.

This work was made possible by grants to A.W.M. from the TESS Guest Investigator Program (80NSSC21K1054), NASA's Astrophysics Data Analysis Program (80NSSC19K0583), and the NSF CAREER grant (AST-2143763). M.L.W. and M.G.B. were supported by the NC Space Grant Graduate Research program. S.N.Q. acknowledges support from the TESS GI Program under award 80NSSC21K1056.

The authors extend many thanks to Patricio, Carlos, Juan, Sergio, and Rodrigo at SOAR for helping through many nights of observations.

This research includes data from observations obtained at the Southern Astrophysical Research (SOAR) telescope, which is a joint project of the Ministério da Ciência, Tecnologia e Inovações (MCTI/LNA) do Brasil, the US National Science Foundation's NOIRLab, the University of North Carolina at Chapel Hill (UNC), and Michigan State University (MSU).

This paper includes data collected by the TESS mission, which are publicly available from the Mikulski Archive for Space Telescopes (MAST). Funding for the TESS mission is provided by NASA's Science Mission Directorate. We acknowledge the use of public TOI Release data from pipelines at the TESS Science Office and at the TESS Science Processing Operations Center.

The Exoplanet Follow-up Observing Program (ExoFOP) website is designed to optimize resources and facilitate collaboration in follow-up studies of exoplanet candidates. ExoFOP-TESS serves as a repository for community-gathered follow-up data on TESS (Transiting Exoplanet Survey Satellite) planet candidates by allowing the upload and display of data and derived astrophysical parameters.

This data set or service is made available by the NASA Exoplanet Science Institute at IPAC, which is operated by the California Institute of Technology under contract with NASA.

This work has made use of data from the European Space Agency (ESA) mission Gaia,[40] processed by the Gaia Data Processing and Analysis Consortium (DPAC).[41] Funding for the DPAC has been provided by national institutions, in particular the institutions participating in the Gaia Multilateral Agreement.

This research has made use of the VizieR catalog access tool, CDS, Strasbourg, France. The original description of the VizieR service was published in A&AS 143, 23. Resources supporting this work were provided by the NASA High-End Computing (HEC) Program through the NASA Advanced Supercomputing (NAS) Division at Ames Research Center for the production of the SPOC data products.

This work makes use of observations from the LCOGT NRES network.

Observations in the paper made use of the High-Resolution Imaging instrument(s) Zorro. Zorro was funded by the NASA Exoplanet Exploration Program and built at the NASA Ames Research Center by Steve B. Howell, Nic Scott, Elliott P. Horch, and Emmett Quigley. Zorro was mounted on the Gemini South telescope of the international Gemini Observatory, a program of NSF's NOIRLab, which is managed by the Association of Universities for Research in Astronomy (AURA) under a cooperative agreement with the National Science Foundation. On behalf of the Gemini partnership: the National Science Foundation (United States), National Research Council (Canada), Agencia Nacional de Investigación y Desarrollo (Chile), Ministerio de Ciencia, Tecnología e Innovación (Argentina), Ministério da Ciência, Tecnologia e Inovações (Brazil), and Korea Astronomy and Space Science Institute (Republic of Korea).

This work is based on observations made with the Italian Telescopio Nazionale Galileo (TNG) operated by the Fundación Galileo Galilei (FGG) of the Istituto Nazionale di Astrofisica (INAF) at the Observatorio del Roque de los Muchachos (La Palma, Canary Islands, Spain). Part of this research was carried out at the Jet Propulsion Laboratory, California Institute of Technology, under a contract with NASA. The HARPS-N project has been funded by the Prodex Program of the Swiss Space Office (SSO), the Harvard University Origins of Life Initiative (HUOLI), the Scottish Universities Physics Alliance (SUPA), the University of Geneva, the Smithsonian Astrophysical Observatory (SAO), and the Italian National Astrophysical Institute (INAF), the University of St Andrews, Queens University Belfast, and the University of Edinburgh. D.J.A. acknowledges support from the STFC via an Ernest Rutherford Fellowship (ST/R00384X/1). The work of H.P.O. has been carried out within the framework of the NCCR PlanetS supported by the Swiss National Science Foundation under grants 51NF40_182901 and 51NF40_205606.

Facilities: TESS, SOAR 4 m (Goodman HTS), LCOGT 1 m (NRES), SMARTS 1.5 m (CHIRON), TNG (HARPS-N), Gemini South (Zorro).

Software: Astropy (Astropy Collaboration et al. 2013, 2018), Astroquery (Ginsburg et al. 2019), matplotlib (Hunter 2007), `corner.py` (Foreman-Mackey 2016), Comove (Tofflemire et al. 2021), `BANYAN` Σ (Malo et al. 2012; Gagné et al. 2018), BANZAI-NRES, `misttborn.py` (Mann et al. 2016a; Johnson et al. 2018), *emcee* (Foreman-Mackey et al. 2013), *batman* (Kreidberg 2015), `celerite` (Foreman-Mackey et al. 2017), `triceratops` (Giacalone et al. 2021), `MOLUSC` (Wood et al. 2021).

[40] https://www.cosmos.esa.int/gaia

[41] https://www.cosmos.esa.int/web/gaia/dpac/consortium

Appendix A
BANYAN Definitions of LCC Subpopulations

Since MELANGE-4 is near to several other young moving groups, correctly defining this new population requires not only a description of it, but also an accurate description of the nearby groups. Since the publication of Gagné et al. (2018), significant substructure has been found within, e.g., LCC (Pecaut & Mamajek 2016; Goldman et al. 2018; Kerr et al. 2021). Some of the LCC subpopulations found by Goldman et al. (2018) and Kerr et al. (2021) are near MELANGE-4 (spatially and kinematically), raising the risk of contamination. To handle this, we defined each of the populations as a separate moving group within BANYAN Σ, which should provide a more accurate relative probability of membership between groups.

The LCC subpopulations were independently found by G18 and K21, who used different naming schemes for the groups. We use the names from G18, and note that the groups A0,[42] A, B, and C correspond to B, C, E and D in K21. K21's group LCC A has no counterpart in the Goldman paper, but is more commonly known as ϵ Chamaeleontis, and was already in BANYAN Σ.

First we define the membership of the LCC subpopulations by combining the membership lists from G18 and K21. We obtain the candidate members of groups A0, A, B, and C from Table 2 of G18, and use the provided Gaia DR2 coordinates to cross-match the sources with Gaia DR3, searching a 1′ area around each star, and taking the closest source as a match. The K21 candidate members are obtained from Table 3 of K21, and the provided Gaia DR2 coordinates are used to cross-match the sources with Gaia eDR3, using the same radius as for the G18 match. We then combine the membership lists for the two, using their Gaia DR3 source IDs.

For subpopulations A0, A, and B, the majority of the candidate members were recovered by both surveys, and the selections of each are similar, with a common core, and some variation on the outskirts. However, few of the subpopulation C candidates were recovered by K21, so that the G18 membership list contains the vast majority of the members, and has a significantly larger extent than the K21 membership.

To calculate the center vector and covariance matrix of each subpopulation, we use the combined membership lists, cut to only those stars with Gaia DR2 RV measurements. The covariance matrices of all four populations are shown below, and the values of the center vector are listed in Table 7.

Musca (LCC-A0)

$$\bar{\bar{\Sigma}}_{A0} = \begin{bmatrix} 6.774 & -3.706 & 12.025 & 1.906 & -2.431 & 1.222 \\ -3.706 & 13.499 & -1.037 & 5.263 & -7.798 & -1.359 \\ 12.025 & -1.037 & 27.141 & 9.426 & -13.696 & 1.53 \\ 1.906 & 5.263 & 9.426 & 19.13 & -30.034 & -3.405 \\ -2.431 & -7.798 & -13.696 & -30.034 & 47.339 & 5.521 \\ 1.222 & -1.359 & 1.53 & -3.405 & 5.521 & 1.094 \end{bmatrix}.$$

LCC-A

$$\bar{\bar{\Sigma}}_{A} = \begin{bmatrix} 5.364 & -0.873 & -0.807 & 0.165 & 0.614 & 0.16 \\ -0.873 & 17.4 & -4.569 & 1.271 & -0.026 & -0.283 \\ -0.807 & -4.569 & 9.034 & 0.815 & -1.742 & 0.378 \\ 0.165 & 1.271 & 0.815 & 5.792 & -9.457 & -0.28 \\ 0.614 & -0.026 & -1.742 & -9.457 & 16.059 & 0.449 \\ 0.16 & -0.283 & 0.378 & -0.28 & 0.449 & 0.149 \end{bmatrix}.$$

LCC-B

$$\bar{\bar{\Sigma}}_{B} = \begin{bmatrix} 54.486 & 3.078 & -4.913 & 1.8 & 3.413 & -0.675 \\ 3.078 & 16.729 & -4.972 & 0.169 & 1.887 & -0.477 \\ -4.913 & -4.972 & 28.202 & 0.205 & -1.079 & 2.185 \\ 1.8 & 0.169 & 0.205 & 2.052 & -3.02 & 0.348 \\ 3.413 & 1.887 & -1.079 & -3.02 & 6.021 & -0.673 \\ -0.675 & -0.477 & 2.185 & 0.348 & -0.673 & 0.392 \end{bmatrix}.$$

LCC-C

$$\bar{\bar{\Sigma}}_{C} = \begin{bmatrix} 114.137 & 4.809 & 5.911 & 7.288 & 0.418 & 0.815 \\ 4.809 & 44.83 & -7.989 & 1.304 & 3.228 & -1.043 \\ 5.911 & -7.989 & 16.065 & 0.677 & -0.809 & 0.81 \\ 7.288 & 1.304 & 0.677 & 3.529 & -3.895 & 0.911 \\ 0.418 & 3.228 & -0.809 & -3.895 & 6.345 & -1.198 \\ 0.815 & -1.043 & 0.81 & 0.911 & -1.198 & 0.58 \end{bmatrix}.$$

We add the groups to BANYAN Σ using the parameters listed above. To test the recovery of the initial samples, we run BANYAN Σ on a sample of stars from Gaia EDR3 within 100 pc of the central position of LCC (using the original definition from Gagné et al. 2018). We use all resulting candidates with a kinematic membership probability greater than 50% as the output sample for each population.

We recover a majority of the input stars for all four populations, with A0 having the lowest recovery rate at 56%, and C having the highest, recovering 92% of the initial sample.

[42] Also known as Musca (Mann et al. 2022).

Table 5
Members of MELANGE-4

DR3 ID	R.A. (°)	Decl. (°)	π (mas)	RUWE	G	$G_{BP} - G_{RP}$	K_S	FF[a]	P_{BANYAN}	TIC
Gaia DR3 5269346361575307264	121.3139	−71.103	10.750	0.927	11.62	1.71	8.782		0.815	TIC306779173
Gaia DR3 5314992445071183872	130.1828	−57.550	13.887	1.354	14.22	2.74	10.338		0.554	TIC45192378
Gaia DR3 5215182391566488448	135.4216	−77.933	11.519	1.112	15.12	2.89	11.254		0.868	TIC323574677
Gaia DR3 5304828971900544896	136.2097	−56.294	12.413	1.159	12.64	2.15	9.334		0.706	TIC384397468
Gaia DR3 5216186726719969792	139.3644	−74.734	13.090	1.070	5.86	−0.03	5.865		0.921	TIC452468734
Gaia DR3 5219515292014933760	139.6958	−70.615	10.086	1.078	15.67	3.13	11.636		0.540	TIC303693668
Gaia DR3 5217812354662194048	140.9457	−73.682	13.088	1.227	13.38	2.62	9.722		0.555	TIC452522877
Gaia DR3 5250471114189790336	141.6836	−63.023	11.940	2.249	14.26	2.94	10.325		0.546	TIC360130454
Gaia DR3 5219351911459314048	142.6309	−70.697	9.854	0.944	10.08	0.89	8.565		0.755	TIC370330200
Gaia DR3 5217846851839896832	142.8546	−73.747	12.832	1.589	9.19	0.80	⋯		0.815	TIC843283158
Gaia DR3 5217846817480160640	142.9057	−73.751	12.804	1.966	13.90	3.13	9.823		0.728	TIC452591875
Gaia DR3 5217554622264363008	143.5176	−74.093	12.853	1.277	14.29	2.89	10.379		0.729	TIC452604601
Gaia DR3 5250926999202194688	143.8354	−62.367	12.017	1.206	14.45	2.86	10.552		0.730	TIC361227905
Gaia DR3 5251098523021221376	144.8372	−61.328	14.479	0.791	4.48	−0.07	4.647		0.723	TIC361834361
Gaia DR3 5244271552233795200	145.1523	−67.755	13.104	1.108	16.46	3.81	11.824		0.618	TIC370825476
Gaia DR3 5307852908070273792	145.5575	−56.027	12.422	1.128	14.39	2.94	10.47		0.598	TIC441744406
Gaia DR3 5218453026345066368	147.2531	−71.634	12.754	2.566	13.90	2.55	9.5		0.582	TIC371372421
Gaia DR3 5257836605156299776	147.5025	−58.472	12.876	1.163	14.23	2.88	10.393		0.537	TIC444536794
Gaia DR3 5218262707753445760	147.6715	−71.783	11.126	1.111	14.79	2.94	10.878		0.887	TIC371498920
Gaia DR3 5257392295070412032	148.5564	−60.275	11.835	1.070	12.32	2.03	9.083		0.952	TIC269691345
Gaia DR3 5259151277454731008	149.3857	−58.390	10.059	14.572	15.49	3.31	⋯		0.509	TIC855167492
Gaia DR3 5258252942105518080	150.9937	−59.401	10.204	1.285	14.23	2.93	10.285		0.552	TIC462320070
Gaia DR3 5230321567172871040	151.3447	−71.616	11.583	2.216	14.60	2.93	10.674		0.968	TIC372515585
Gaia DR3 5230321361014440704	151.3556	−71.624	11.671	5.079	12.45	2.56	8.802		0.952	TIC372515598
Gaia DR3 5253295141117135104	152.1298	−61.633	12.623	1.138	15.46	2.96	11.453		0.743	TIC375752627
Gaia DR3 5246284685000163968	152.6949	−65.380	9.227	1.214	12.94	2.02	9.756		0.502	TIC376031475
Gaia DR3 5254979283697117440	154.0168	−59.909	12.276	1.225	13.88	2.73	9.483		0.966	TIC463556306
Gaia DR3 5255082603415689600	154.3064	−59.640	12.378	1.181	15.42	3.23	11.297		0.968	TIC463578988
Gaia DR3 5251591482193147776	154.7628	−64.681	11.521	1.303	13.38	2.51	9.807		0.978	TIC378035942
Gaia DR3 5251591477884660352	154.7696	−64.676	11.567	1.119	6.48	0.08	⋯		0.844	TIC847861519

Note.
[a] Friends are less than 30 pc away and a tangential velocity within 3 km s^{-1} of HD 109833.

(This table is available in its entirety in machine-readable form.)

Table 6
Observations of MELANGE-4 Candidates

Name	SpT	Telescope	ObsDate YYYYMMDD	M_K mag	EW(Li) mÅ	$P_{\rm BANYAN}$
TIC 427036962	M3	Goodman/SOAR	20210329, 20210919	6.52	413.0	0.961
TIC 258101273	M1	Goodman/SOAR	20210329	4.83	29.0	0.979
TIC 259726904	M3	Goodman/SOAR	20210329	5.01	<10	0.997
TIC 68515382	M3	Goodman/SOAR	20210423	6.09	153.0	0.993
TIC 378413560	M3	Goodman/SOAR	20210423	4.98	<10	0.902
TIC 253067348	M4	Goodman/SOAR	20210423	6.38	680.0	0.992
TIC 303048907	M4	Goodman/SOAR	20210423	5.90	<10	0.928
TIC 378126824	M3	Goodman/SOAR	20210423	5.27	20.0	0.852
TIC 406249571	M3	Goodman/SOAR	20210423	5.73	583.0	0.986
TIC 401561267	M3	Goodman/SOAR	20210501	5.42	34.0	0.962
TIC 453766186	M3	Goodman/SOAR	20210501	5.63	<10	0.896
TIC 453808153	M3	Goodman/SOAR	20210501	5.78	<10	0.934
TIC 401484858	M1	Goodman/SOAR	20210507	6.11	16.0	0.986
TIC 402030604	M3	Goodman/SOAR	20210507	5.72	<10	0.897
TIC 335366271	M3	Goodman/SOAR	20210507	5.93	33.0	0.998
TIC 451425923	M1	Goodman/SOAR	20210507	6.23	<10	0.821
TIC 402808278	M3	Goodman/SOAR	20210507, 20210810	5.70	<10	0.504
TIC 425871236	M3	Goodman/SOAR	20210810	5.53	<10	0.974
TIC 299610396	M3	Goodman/SOAR	20210810	5.78	<10	0.891
TIC 97882429	M3	Goodman/SOAR	20210810	5.84	<10	0.663
Gaia5227091236372916864	M4	Goodman/SOAR	20210810	6.09	414.0	0.996
TIC256168939	M3	Goodman/SOAR	20210810	5.89	204.0	0.979
TIC189421351	M0	Goodman/SOAR	20210919	4.07	313.0	0.728
TIC461148251	M3	Goodman/SOAR	20210919	5.17	<10	0.882
TIC443273186	M3	Goodman/SOAR	20210920	6.90	<10	0.985
TIC361571108	M5	Goodman/SOAR	20210920	6.87	456.0	0.958
TYC 9034-968-1	K2	CHIRON/SMARTS	20210430	3.70	250.0	0.999
TYC 8992-346-1		CHIRON/SMARTS	20210504	3.34	340.0	0.999

Table 7
Parameters of LCC Subpopulations

Goldman Name	Kerr Name	$N_{\rm Goldman}$	$N_{\rm Kerr}$	$N_{\rm Total}$	X (pc)	Y(pc) (pc)	Z (pc)	U (km s^{-1})	V (km s^{-1})	W (km s^{-1})	Age (Myr)
A0	B	49	70	79	52	−87	−15	−8.48	−21.69	−8.88	10.6 ± 1.9
A	C	149	197	211	53	−91	−3	−9.80	−19.71	−7.79	12.0 ± 1.8
B	E	317	441	474	53	−94	11	−8.92	−20.30	−6.88	14.9 ± 1.6
C	D	487	69	494	61	−96	22	−8.55	−20.36	−6.14	16.6 ± 1.1

The A0 population has the smallest number of stars, and only a fraction of them have radial-velocity measurements on which to base the BANYAN Σ definition, a likely contributor to the lower recovery fraction. For subpopulations A, B, and C, the recovery rates were >75%. Many of the stars that are not recovered are placed into a different subpopulation (so still part of LCC). In particular, there was significant cross-contamination between groups A and B, and between groups B and C. This was expected, as both groups show significant overlap in spatial and kinematic space, and it is likely the input lists were imperfect.

Appendix B
Revised Ages of the LCC Subgroups

Our determination that MELANGE-4 is not part of the known LCC subgroups was based on differences in both kinematics and age. The latter is complicated by the discrepant age in the literature; Goldman et al. (2018) assigned ages of 7–10 Myr for all populations while Kerr et al. (2021) found ages ranging from 13–23 Myr for the same groups. Using the Kerr et al. (2021) ages, the oldest group is marginally consistent with our age for MELANGE-4 (25–30 Myr). These differences are likely a reflection of differences in methodology and models, as is evident by the fact that both references agree on ordering of groups in terms of age.

To ensure a more robust comparison, we place the ages of each population on a consistent scale as was done for MELANGE-4 in Section 4.4. We adopt a target selection for each of the four subgroups using our updated BANYAN Σ model described in Section A. We then fit each group using a mixture identical to what was described in Section 4.4 and Mann et al. (2022). For simplicity, we restrict our analysis to

the PARSEC models and solar metallicity. All fits are run with 20 walkers until they passed 50 times the autocorrelation time (checking every 5000 steps), for a total of 10,000–30,000 steps.

In all cases, our ages are between the values from Goldman et al. (2018) and Kerr et al. (2021). We summarize the results in Table 7. Importantly, we find that the oldest group is 16.6 ± 1.1 Myr, inconsistent with our identically derived isochronal age (26.0 ± 2.1 Myr) and our LDB age for MELANGE-4.

Our fits are mildly sensitive to membership selection, assumed metallicity, or the model grid. Using the original membership list from Goldman et al. (2018) or Kerr et al. (2021) changes our ages at the 1–2 Myr level, small compared to the difference between the two literature ages (5–13 Myr). Adjusting the assumed metallicity at the 0.1 dex level or swapping to the DSEP magnetic models also changes the derived ages by $\lesssim$2 Myr, but impacted all groups in the same direction (including MELANGE-4).

ORCID iDs

Mackenna L. Wood https://orcid.org/0000-0001-7336-7725
Andrew W. Mann https://orcid.org/0000-0003-3654-1602
Madyson G. Barber https://orcid.org/0000-0002-8399-472X
Jonathan L. Bush https://orcid.org/0000-0002-9446-9250
Adam L. Kraus https://orcid.org/0000-0001-9811-568X
Benjamin M. Tofflemire https://orcid.org/0000-0003-2053-0749
Andrew Vanderburg https://orcid.org/0000-0001-7246-5438
Elisabeth R. Newton https://orcid.org/0000-0003-4150-841X
Gregory A. Feiden https://orcid.org/0000-0002-2012-7215
George Zhou https://orcid.org/0000-0002-4891-3517
Luke G. Bouma https://orcid.org/0000-0002-0514-5538
Samuel N. Quinn https://orcid.org/0000-0002-8964-8377
David J. Armstrong https://orcid.org/0000-0002-5080-4117
Ares Osborn https://orcid.org/0000-0002-5899-7750
Vardan Adibekyan https://orcid.org/0000-0002-0601-6199
Elisa Delgado Mena https://orcid.org/0000-0003-4434-2195
Sergio G. Sousa https://orcid.org/0000-0001-9047-2965
Jonathan Gagné https://orcid.org/0000-0002-2592-9612
Matthew J. Fields https://orcid.org/0000-0002-9641-3138
Reilly P. Milburn https://orcid.org/0000-0002-1312-3590
Pa Chia Thao https://orcid.org/0000-0001-5729-6576
Crystal L. Gnilka https://orcid.org/0000-0003-2519-6161
Steve B. Howell https://orcid.org/0000-0002-2532-2853
Nicholas M. Law https://orcid.org/0000-0001-9380-6457
Carl Ziegler https://orcid.org/0000-0002-0619-7639
César Briceño https://orcid.org/0000-0001-7124-4094
George R. Ricker https://orcid.org/0000-0003-2058-6662
Roland Vanderspek https://orcid.org/0000-0001-6763-6562
David W. Latham https://orcid.org/0000-0001-9911-7388
Sara Seager https://orcid.org/0000-0002-6892-6948
Joshua N. Winn https://orcid.org/0000-0002-4265-047X
Jon M. Jenkins https://orcid.org/0000-0002-4715-9460
Joshua E. Schlieder https://orcid.org/0000-0001-5347-7062
Hugh P. Osborn https://orcid.org/0000-0002-4047-4724
Joseph D. Twicken https://orcid.org/0000-0002-6778-7552
David R. Ciardi https://orcid.org/0000-0002-5741-3047
Chelsea X. Huang https://orcid.org/0000-0003-0918-7484

References

Adibekyan, V., Figueira, P., Santos, N. C., et al. 2015, A&A, 583, A94
Adibekyan, V. Z., Sousa, S. G., Santos, N. C., et al. 2012, A&A, 545, A32
Aller, A., Lillo-Box, J., Jones, D., Miranda, L. F., & Barceló Forteza, S. 2020, A&A, 635, A128
Andrews, J. J., Curtis, J. L., Chanamé, J., et al. 2022, AJ, 163, 275
Asplund, M., Grevesse, N., Sauval, A. J., & Scott, P. 2009, ARA&A, 47, 481
Astropy Collaboration, Price-Whelan, A. M., Sipocz, B. M., et al. 2018, AJ, 156, 123
Astropy Collaboration, Robitaille, T. P., Tollerud, E. J., et al. 2013, A&A, 558, A33
Baraffe, I., & Chabrier, G. 2010, A&A, 521, A44
Baraffe, I., Homeier, D., Allard, F., & Chabrier, G. 2015, A&A, 577, A42
Barber, M. G., Mann, A. W., Bush, J. L., et al. 2022, AJ, 164, 88
Bell, C. P. M., Mamajek, E. E., & Naylor, T. 2015, MNRAS, 454, 593
Belokurov, V., Penoyre, Z., Oh, S., et al. 2020, MNRAS, 496, 1922
Benatti, S., Nardiello, D., Malavolta, L., et al. 2019, arXiv:1904.01591 [astro-ph]
Binks, A. S., & Jeffries, R. D. 2014, MNRAS: Letters, 438, L11
Binks, A. S., Jeffries, R. D., Jackson, R. J., et al. 2021, MNRAS, 505, 1280
Bochanski, J. J., West, A. A., Hawley, S. L., & Covey, K. R. 2007, AJ, 133, 531
Bohn, A. J., Ginski, C., Kenworthy, M. A., et al. 2021, A&A, 648, A73
Bohn, A. J., Kenworthy, M. A., Ginski, C., et al. 2020a, ApJ, 898, L16
Bohn, A. J., Kenworthy, M. A., Ginski, C., et al. 2020b, MNRAS, 492, 431
Booth, M., del?Burgo, C., & Hambaryan, V. V. 2021, MNRAS, 500, 5552
Bouma, L. G., Kerr, R., Curtis, J. L., et al. 2022, AJ, 164, 215
Bressan, A., Marigo, P., Girardi, L., et al. 2012, MNRAS, 427, 127
Buchhave, L. A., Latham, D. W., Johansen, A., et al. 2012, Natur, 486, 375
Burke, C. J., Pinsonneault, M. H., & Sills, A. 2004, ApJ, 604, 272
Cao, L., Pinsonneault, M. H., Hillenbrand, L. A., & Kuhn, M. A. 2022, ApJ, 924, 84
Cardelli, J. A., Clayton, G. C., & Mathis, J. S. 1989, ApJ, 345, 245
Castelli, F., & Kurucz, R. L. 2004, arXiv:astro-ph/0405087
Chiozzi, G., Guzman, J. C., Jenkins, J. M., et al. 2016, Proc. SPIE, 9913, 99133E
Clemens, J. C., Crain, J. A., & Anderson, R. 2004, Proc. SPIE, 5492, 331
Costa Silva, A. R., Delgado Mena, E., & Tsantaki, M. 2020, A&A, 634, A136
Currie, T., Biller, B., Lagrange, A.-M., et al. 2022, arXiv:2205.05696
da Silva, L., Torres, C. A. O., de la Reza, R., et al. 2009, A&A, 508, 833
David, T. J., Hillenbrand, L. A., Petigura, E. A., et al. 2016, Natur, 534, 658
David, T. J., Petigura, E. A., Luger, R., et al. 2019, ApJL, 885, L12
De Rosa, R. J., Rameau, J., Patience, J., et al. 2016, ApJ, 824, 121
de Zeeuw, P. T., Hoogerwerf, R., Bruijne, J. H. J. d., Brown, A. G. A., & Blaauw, A. 1999, AJ, 117, 354
Donati, J. F., Moutou, C., Malo, L., et al. 2016, Natur, 534, 662
Donati, J.-F., Semel, M., Carter, B. D., Rees, D. E., & Cameron, A. C. 1997, MNRAS, 291, 658
Dotter, A., Chaboyer, B., Jevremovic, D., et al. 2008, ApJS, 178, 89
Doyle, A. P., Davies, G. R., Smalley, B., Chaplin, W. J., & Elsworth, Y. 2014, MNRAS, 444, 3592
Espinoza, N., & Jordán, A. 2015, MNRAS, 450, 1879
Feiden, G. A. 2016, A&A, 593, A99
Feinstein, A. D., David, T. J., Montet, B. T., et al. 2022, ApJ, 925, L2
Foreman-Mackey, D., Agol, E., Ambikasaran, S., & Angus, R. 2017, AJ, 154, 220
Foreman-Mackey, D., Hogg, D. W., Lang, D., & Goodman, J. 2013, PASP, 125, 306
Foreman-Mackey, D. 2016, corner.py: Scatterplot matrices in Python, doi:10.21105/joss.00024
Freund, S., Czesla, S., Robrade, J., Schneider, P. C., & Schmitt, J. H. M. M. 2022, A&A, 664, A105
Gagné, J., David, T. J., Mamajek, E. E., et al. 2020, ApJ, 903, 96
Gagné, J., Faherty, J. K., Moranta, L., & Popinchalk, M. 2021, ApJL, 915, L29
Gagné, J., Mamajek, E. E., Malo, L., et al. 2018, ApJ, 856, 23
Gaia Collaboration, Brown, A. G. A., Vallenari, A., et al. 2021, A&A, 649, A1
Gaia Collaboration, Prusti, T., Bruijne, J. H. J. d., et al. 2016, A&A, 595, A1
Gaia Collaboration, Vallenari, A., Brown, A. G. A., & Prusti, T. 2022, A&A,
Gaidos, E., & Mann, A. W. 2014, ApJ, 791, 54
Giacalone, S., Dressing, C. D., Jensen, E. L. N., et al. 2021, AJ, 161, 24
Ginsburg, A., Sipocz, B. M., Brasseur, C. E., et al. 2019, AJ, 157, 98
Goldman, B., Röser, S., Schilbach, E., Moór, A. C., & Henning, T. 2018, ApJ, 868, 32

Gray, R. O., & Corbally, C. J. 1994, AJ, 107, 742
Grevesse, N., & Sauval, A. J. 1998, SSRv, 85, 161
Guerrero, N. M., Seager, S., Huang, C. X., et al. 2021, ApJS, 254, 39
Gully-Santiago, M. A., Herczeg, G. J., Czekala, I., et al. 2017, ApJ, 836, 200
Gutiérrez Albarrán, M. L., Montes, D., Gómez Garrido, M., et al. 2020, A&A, 643, A71
Haisch, K. E., Jr., Lada, E. A., & Lada, C. J. 2001, ApJ, 553, L153
Hattori, S., Foreman-Mackey, D., Hogg, D. W., et al. 2021, arXiv:2106.15063
Heap, S. R., & Lindler, D. 2016, in ASP Conf. Ser. 503, The Science of Calibration, ed. S. Deustua et al. (San Francisoc, CA: ASP), 211
Hinkley, S., Kraus, A. L., Ireland, M. J., et al. 2015, ApJL, 806, L9
Høg, E., Fabricius, C., Makarov, V. V., et al. 2000, A&A, 355, L27
Hogg, D. W., Bovy, J., & Lang, D. 2010, arXiv:1008.4686
Howell, S. B., Everett, M. E., Sherry, W., Horch, E., & Ciardi, D. R. 2011, AJ, 142, 19
Huang, C. X., Vanderburg, A., Pal, A., et al. 2020, RNAAS, 4, 204
Hunter, J. D. 2007, CSE, 9, 90
Husser, T.-O., von Berg, S. W., Dreizler, S., et al. 2013, A&A, 553, A6
Jenkins, J. M. 2002, ApJ, 575, 493
Jenkins, J. M., Radziwill, N. M., Bridger, A., et al. 2010, Proc. SPIE, 7740, 77400D
Jenkins, J. M., Tenenbaum, P., Seader, S., et al. 2020, Kepler Data Processing Handbook: Transiting Planet Search, Kepler Science Document, KSCI-19081-003
Johnson, M. C., Dai, F., Justesen, A. B., et al. 2018, MNRAS, 481, 596
Kapteyn, J. C. 1914, ApJ, 40, 43
Kerr, R. M. P., Rizzuto, A. C., Kraus, A. L., & Offner, S. S. R. 2021, ApJ, 917, 23
Kipping, D. M. 2013, MNRAS, 435, 2152
Klein, B., Zicher, N., Kavanagh, R. D., et al. 2022, MNRAS, 512, 5067
Kounkel, M., Covey, K., Moe, M., et al. 2019, AJ, 157, 196
Kraus, A. L., Cody, A. M., Covey, K. R., et al. 2015, ApJ, 807, 3
Kraus, A. L., Herczeg, G. J., Rizzuto, A. C., et al. 2017, ApJ, 838, 150
Kraus, A. L., Shkolnik, E. L., Allers, K. N., & Liu, M. C. 2014, AJ, 147, 146
Kreidberg, L. 2015, PASP, 127, 1161
Krolikowski, D. M., Kraus, A. L., & Rizzuto, A. C. 2021, AJ, 162, 110
Kurucz, R. L. 1993a, SYNTHE spectrum synthesis programs and line data
Kurucz, R. L. 1993, Int. Astronomical Union Coll. 138, 44 (Trieste, Italy), 87
Li, J., Tenenbaum, P., Twicken, J. D., et al. 2019, PASP, 131, 024506
Lim, P. L. 2020, doi:10.5281/zenodo.3971036
Lindegren, L., Klioner, S. A., Hernández, J., et al. 2021, A&A, 649, A2
Lissauer, J. J., Marcy, G. W., Rowe, J. F., et al. 2012, ApJ, 750, 112
Lomb, N. R. 1976, Ap&SS, 39, 447
Madsen, S., Dravins, D., & Lindegren, L. 2002, A&A, 381, 446
Malo, L., Doyon, R., Lafrenière, D., et al. 2012, ApJ, 762, 88
Mamajek, E. E., & Bell, C. P. M. 2014, MNRAS, 445, 2169
Mamajek, E. E., Meyer, M. R., & Liebert, J. 2002, AJ, 124, 1670
Mann, A. W., Dupuy, T., Kraus, A. L., et al. 2019, ApJ, 871, 63
Mann, A. W., Gaidos, E., Mace, G. N., et al. 2016a, ApJ, 818, 46
Mann, A. W., Newton, E. R., Rizzuto, A. C., et al. 2016b, AJ, 152, 61
Mann, A. W., Wood, M. L., Schmidt, S. P., et al. 2022, AJ, 163, 156
Masuda, K., & Winn, J. N. 2020, AJ, 159, 81
McInnes, L., & Healy, J. 2017, arXiv:1705.07321
Meingast, S., Alves, J., & Fürnkranz, V. 2019, A&A, 622, L13
Messina, S., Nardiello, D., Desidera, S., et al. 2022, A&A, 657, L3
Moór, A., Ábrahám, P., Kóspál, Á., et al. 2013, ApJL, 775, L51
Morton, T. D. 2015, isochrones: Stellar Model Grid Package, Astrophysics Source Code Library, ascl:1503.010
Murphy, S. J., Lawson, W. A., & Bessell, M. S. 2013, MNRAS, 435, 1325
Newton, E. R., Mann, A. W., Tofflemire, B. M., et al. 2019, ApJ, 880, L17
Newton, E. R., Rampalli, R., Kraus, A. L., et al. 2022, AJ, 164, 115
Oh, S., Price-Whelan, A. M., Hogg, D. W., Morton, T. D., & Spergel, D. N. 2017, AJ, 153, 257
Parviainen, H., & Aigrain, S. 2015, MNRAS, 453, 3821
Pecaut, M. J., & Mamajek, E. E. 2013, ApJS, 208, 9
Pecaut, M. J., & Mamajek, E. E. 2016, MNRAS, 461, 794
Pecaut, M. J., Mamajek, E. E., & Bubar, E. J. 2012, ApJ, 746, 154
Phillips, M. W., Tremblin, P., Baraffe, I., et al. 2020, A&A, 637, A38
Poppenhaeger, K., Ketzer, L., & Mallonn, M. 2021, MNRAS, 500, 4560
Preibisch, T., & Mamajek, E. 2008, in Handbook of Star Forming Regions, Volume II, ed. B. Reipurth, Vol. 5 (San Francisco, CA: ASP), 235
Press, W. H., & Rybicki, G. B. 1989, ApJ, 338, 277
Rameau, J., Chauvin, G., Lagrange, A.-M., et al. 2013, ApJ, 779, L26
Rampalli, R., Agüeros, M. A., Curtis, J. L., et al. 2021, ApJ, 921, 167
Rayner, J. T., Cushing, M. C., & Vacca, W. D. 2009, ApJS, 185, 289
Rebull, L. M., Stauffer, J. R., Cody, A. M., et al. 2018, AJ, 155, 196
Ricker, G. R., Winn, J. N., Vanderspek, R., et al. 2015, JATIS, 1, 014003
Riello, M., Angeli, F. D., Evans, D. W., et al. 2021, A&A, 649, A3
Rizzuto, A. C., Ireland, M. J., & Robertson, J. G. 2011, MNRAS, 416 3108
Rizzuto, A. C., Mann, A. W., Vanderburg, A., Kraus, A. L., & Covey, K. R. 2017, AJ, 154, 224
Rizzuto, A. C., Newton, E. R., Mann, A. W., et al. 2020, AJ, 160, 33
Rockcliffe, K. E., Newton, E. R., Youngblood, A., et al. 2021, AJ, 162, 116
Santos, N. C., Sousa, S. G., Mortier, A., et al. 2013, A&A, 556, A150
Savanov, I. S., Dmitrienko, E. S., Karmakar, S., & Pandey, J. C. 2018, ARep, 62, 532
Scargle, J. D. 1982, ApJ, 263, 835
Scott, N. J., Howell, S. B., Gnilka, C. L., et al. 2021, FrASS, 8, 138
Seager, S., & Mallén-Ornelas, G. 2003, ApJ, 585, 1038
Sergison, D. J., Mayne, N. J., Naylor, T., Jeffries, R. D., & Bell, C. P. M. 2013, MNRAS, 434, 966
Shkolnik, E. L., Allers, K. N., Kraus, A. L., Liu, M. C., & Flagg, L. 2017, AJ, 154, 69
Siverd, R. J., Brown, T. M., Barnes, S., et al. 2018, Proc. SPIE, 10702, 107026C
Skrutskie, M. F., Cutri, R. M., Stiening, R., et al. 2003, 2MASS All-Sky Point Source Catalog, IPAC, doi:10.26131/IRSA2
Skrutskie, M. F., Cutri, R. M., Stiening, R., et al. 2006, AJ, 131, 1163
Smith, J. C., Stumpe, M. C., Van Cleve, J. E., et al. 2012, PASP, 124, 1000
Sneden, C. A. 1973, PhD thesis, The Univ. Texas at Austin
Soderblom, D. R., Hillenbrand, L. A., Jeffries, R. D., Mamajek, E. E., & Naylor, T. 2014, Protostars and Planets VI (Tuscon, AZ: Univ. of Arizona Press), 219
Somers, G., Cao, L., & Pinsonneault, M. H. 2020, ApJ, 891, 29
Somers, G., Pinsonneault, M. H., & Cao, L. 2019, The SPOTS Models: A Grid of Theoretical Stellar Evolution Tracks and Isochrones For Testing The Effects of Starspots on Structure and Colors, v1.0, Zenodo, doi:10.5281/zenodo.3593339
Sousa, S. G. 2014, arXiv:1407.5817
Sousa, S. G., Santos, N. C., Adibekyan, V., Delgado-Mena, E., & Israelian, G. 2015, A&A, 577, A67
Stassun, K. G., Feiden, G. A., & Torres, G. 2014, NewAR, 60, 1
Stassun, K. G., Oelkers, R. J., Pepper, J., et al. 2018, AJ, 156, 102
Stumpe, M. C., Smith, J. C., Catanzarite, J. H., et al. 2014, PASP, 126, 100
Stumpe, M. C., Smith, J. C., Van Cleve, J. E., et al. 2012, PASP, 124, 985
Tanaka, H., & Ward, W. R. 2004, ApJ, 602, 388
Tayar, J., Claytor, Z. R., Huber, D., & van Saders, J. 2022, ApJ, 927, 31
Tofflemire, B. M., Rizzuto, A. C., Newton, E. R., et al. 2021, AJ, 161, 171
Tokovinin, A. 2018, PASP, 130, 035002
Tokovinin, A., Fischer, D. A., Bonati, M., et al. 2013, PASP, 125, 1336
Torres, C. A. O., Quast, G. R., da Silva, L., et al. 2006, yCat, 460, 695
Torres, C. A. O., Quast, G. R., Melo, C. H. F., & Sterzik, M. F. 2008, Handbook of Star Forming Regions, Vol. II (San Francisco, CA: ASP), 757
Twicken, J. D., Catanzarite, J. H., Clarke, B. D., et al. 2018, PASP, 130, 064502
Vanderburg, A., Huang, C. X., Rodriguez, J. E., et al. 2019, ApJ, 881, L19
Wang, D., Hogg, D. W., Foreman-Mackey, D., & Schölkop, B. 2016, PASP, 128, 094503
Wood, M. L., Mann, A. W., & Kraus, A. L. 2021, AJ, 162, 128
Wright, E. L., Eisenhardt, P. R. M., Mainzer, A. K., et al. 2010, AJ, 140 1868
Wright, E. L., Eisenhardt, P. R. M., Mainzer, A. K., et al. 2019, AllWISE Source Catalog, IPAC, doi:10.26131/IRSA1
Wright, N. J., & Mamajek, E. E. 2018, MNRAS, 476, 381
Zapatero Osorio, M. R., Bejar, V. J. S., Pavlenko, Y., et al. 2002, A&A, 384, 937
Zhang, M., Knutson, H. A., Wang, L., et al. 2022, AJ, 163, 68
Zhou, G., Rodriguez, J. E., Vanderburg, A., et al. 2018, AJ, 156, 93
Zhou, G., Wirth, C. P., Huang, C. X., et al. 2022, AJ, 163, 289
Ziegler, C., Law, N. M., Baranec, C., et al. 2018, AJ, 156, 259
Ziegler, C., Tokovinin, A., Briceño, C., et al. 2019, AJ, 159, 19
Zucker, C., Goodman, A. A., Alves, J., et al. 2022, Natur, 601, 334